International Journal of Heat and Fluid Flow 86 (2020) 108705

Contents lists available at ScienceDirect

International Journal of Heat and Fluid Flow

journal homepage: www.elsevier.com/locate/ijhff

Non-Darcian Bénard convection in eccentric annuli containing spherical particles

Gazy F. Al-Sumaily [a,b,*], Hasanen M. Hussen [c], Wissam H. Alawee [b], Hayder A. Dhahad [b], Mark C. Thompson [a]

[a] Fluids Laboratory for Aeronautical and Industrial Research (FLAIR), Department of Mechanical and Aerospace Engineering, Monash University, Victoria 3800, Australia
[b] Workshop and Training Centre, University of Technology, Baghdad, Iraq
[c] Mechanical Engineering Department, University of Technology, Baghdad, Iraq

ARTICLE INFO

Keywords:
Natural convection
Bénard convection
Laminar flow
Porous medium
Concentric and eccentric annulus

ABSTRACT

In this paper, a numerical investigation of natural convection in a porous medium confined by two horizontal eccentric cylinders is presented. The cylinders are impermeable to fluid motion and retained at uniform different temperatures. While, the annular porous layer is packed with glass spheres and fully-saturated with air, and the cylindrical packed bed is under the condition of local thermal non-equilibrium. The mathematical model describing the thermal and hydrodynamic phenomena consists of the two-phase energy model coupled by the *Brinkman-Forchheimer-extended Darcy* model under the Boussinesq approximation. The non-dimensional derived system of formulations is numerically discretised and solved using the spectral-element method. The investigation is conducted for a constant cylinder/particle diameter ratio (D_i/d) = 30, porosity (ε) = 0.5, and solid/fluid thermal conductivity ratio (k_r) = 38.6. The effects of the vertical, horizontal and diagonal heat source eccentricity ($-0.8 \leqslant e \leqslant 0.8$) and the annulus radius ratio ($1.5 \leqslant RR \leqslant 5.0$) on the temperature and velocity distributions as well as the overall heat dissipation within both the fluid and solid phases, for a broad range of Rayleigh number ($10^4 \leqslant \mathrm{Ra} \leqslant 8 \times 10^7$). The results show that uni-cellular, bi-cellular and tri-cellular flow regimes appear in the vertical eccentric annulus at the higher positive eccentricity $e = 0.8$ as Rayleigh number increases. However, in the diagonal eccentric annulus, the multi-cellular flow regimes are shown to be deformed and the isotherms are particularly distorted when Rayleigh number increases. In contrast, in the horizontal eccentric annulus, it is found that whatever the Rayleigh number is only an uni-cellular flow regime is seen. In addition, it is shown that the fluid flow is always unstable in the diagonal eccentric geometry at $e = 0.8$ for moderate and higher Rayleigh numbers. However, it loses its stability in the vertical eccentric geometry only at two particular cases, while it is always stable in the horizontal eccentric geometry, for all eccentricities and Rayleigh numbers.

1. Introduction

Natural convection is one of the most complicated physical phenomena that describes the operation of thermal energy transfer in fluids driven by buoyancy forces (Hakan, 2007; Hakan et al., 2009; Selimefendigil and Hakan, 2017; Nadezhda et al., 2017; Walid et al., 2017). Natural convection heat transfer in annuli takes place in numerous industrial applications such as within the nuclear, solar, and electric energy fields, as well as in the thermal storage systems. The presence of a fluid between two circular cylinders, concentric or eccentric, at different fixed temperatures generates a complicated buoyancy-driven flow in the existence of a constant gravitational force. If the temperature discrepancy between the cylinders is slight, the energy conveyance will be dominated by diffusion. Therefore, the average Nusselt number stays generally invariable in such conductive flow regime for the entire Rayleigh numbers under a specific critical value. Over this critical Rayleigh number, the thermal convection occurs producing thermal plumes appearing in the annular gap. Natural convection inside annular

* Corresponding author at: Fluids Laboratory for Aeronautical and Industrial Research (FLAIR), Department of Mechanical and Aerospace Engineering, Monash University, Victoria 3800, Australia.
E-mail addresses: gazy.alsumaily@monash.edu (G.F. Al-Sumaily), 20046@uotechnology.edu.iq (H.M. Hussen), 10603@uotechnology.edu.iq (W.H. Alawee), 10592@uotechnology.edu.iq (H.A. Dhahad), mark.thompson@monash.edu (M.C. Thompson).

https://doi.org/10.1016/j.ijheatfluidflow.2020.108705
Received 27 June 2020; Received in revised form 10 September 2020; Accepted 11 September 2020
Available online 13 October 2020

spaces has been analysed extensively, and received much attention in the literature. For example, the authors (Schwalp and de Witt, 1970; Powe et al., 1971; Custer and Shaughnessy, 1977; Charrier-Mojtabi et al., 1979; Keivan et al., 2017) investigated this problem in concentric annuli; while others such as (Darrell and Roger, 1983; Feldman et al., 1982; Ho et al., 1989; Hosseini et al., 2005; Hwang and Jensen, 1991; Koichi et al., 2001; Kuehn and Goldstein, 1976; Projahn et al., 1981; Ratzel et al., 1979; Yao, 1980) investigated the influence of eccentricity on heat transfer for diverse boundary conditions and using various numerical methods.

Briefly, Kuehn and Goldstein (1976) developed a correlation to predict natural convection heat transfer from horizontal cylinder to a fluid within a cylindrical enclosure under quasi-steady conditions utilising a conduction boundary-layer model. Ratzel et al. (1979) examined natural convection in concentric and eccentric annular regions using the finite element procedure. Yao (1980) studied analytically free convection in eccentric annuli employing perturbation techniques with the eccentric area transformed into a unit circle. Projahn et al. (1981) employed the implicit finite difference method with the body-fitted curvilinear coordinate transformations to model free convection flow in eccentric annuli. They reported results for both vertical and horizontal eccentricities, and compared with data presented by Kuehn and Goldstein (1976). The bipolar coordinate transformations were also utilised by Feldman et al. (1982) to calculate developing flow and thermal distributions within an eccentric annular duct. Darrell and Roger (1983) studied numerically natural convection flow within an eccentric annular region between two circular cylinders isothermally heated employing the finite element and pseudo-spectral algorithms with a bipolar coordinate transformation. Ho et al. (1989) studied free convection in eccentric annuli with mixed boundary conditions and presented a correlation for Nusselt number against Rayleigh number. Hwang and Jensen (1991) investigated a convective dispersed flow in an eccentric annulus using the variables separation method. Koichi et al. (2001) examined natural convection in eccentric horizontal annuli between a heated outer elliptical pipe and a cooled inner cylindrical pipe with different orientations. Hosseini et al. (2005) tested natural convection heat transfer in an open-ended vertical eccentric annulus, and observed an optimal value for the eccentricity in which the heat dissipation is maximised.

Natural convection inside cylindrical porous annuli has a large importance in many industrial applications such as underground cable systems, thermal insulations, and thermal energy storages. The case of concentric porous annulus has obtained the much focus in the literature. Caltagirone (1976) conducted the first experimental investigation on porous annulus of constant radius ratio utlising the Christiansen effect to visualise the isotherms in a cylindrical porous layer. Caltagirone was able to observe only bi-cellular flow regime, and therefore he concluded that the multi-cellular structures do not exist when Rayleigh number increases. Later, Rao et al. (1987), Rao et al. (1988) investigated analytically transient natural convection in a horizontal porous concentric annulus in two and three dimensions, respectively, employing the Galerkin method. They obtained three modes of solutions: The first mode always produces a uni-cellular flow which corresponds to the pure conduction state. The second mode corresponds to the disturbance resulting in the thermal field at the summit of the annulus, so a downforward flow is produced to compose a secondary flow, consequently generating a bi-cellular flow. Whereas, the third mode corresponds to the higher temperature disturbance occurred at the top of the annulus, generating a tri-cellular flow at higher Rayleigh numbers. Himasekhar and Bau (1988) focused on studying the behaviour of two-dimensional bifurcation phenomena using the Galerkin method and the regular perturbation expansion techniques. Unique and multiple solutions were obtained, with a possibility to be stable and unstable, relying upon the values of Rayleigh number and radii ratio used. The visualisation experiments of Caltagirone (1976) have been re-conducted by Charrier-Mojtabi et al. (1991) who proved the existence of two-dimensional four-cell flow structures. The numerical works done by Barbosa Mota and Saatdjian (1992), Barbosa Mota and Saatdjian (1994), Barbosa Mota and Saatdjian (1995) examined the effect of radius ratio on the transition of the flow regime and its stability. They showed that the transition from a two-cell to a four-cell flow regime relies on the Darcy-Rayleigh number, whether it increases or decreases.

The diminution in heat transfer resulting from the use of an eccentric geometry was first examined numerically by Bau (1984), Bau (1984) for small and moderate values of Darcy-Rayleigh numbers, respectively, using the regular perturbation expansion technique, and then by Himasekhar and Bau (1986) for large Darcy-Rayleigh numbers using a boundary-layer technique. Their results were utilised to clarify the potential of heat transfer optimisation from an annulus by a correct selection of the eccentricity. In these works, the steady-state Darcy-Oberbeck-Boussinesq's (DOB) model was used, and the calculated flow field was restricted to only a bi-cellular flow pattern. Later, Barbosa Mota and Saatdjian (1997) employed the transient Darcy-Boussinesq's model and found out that the eccentricity that reduces the heat loss for a particular Rayleigh number and radius ratio alters considerably the flow regime. The results showed that at the eccentricity $e<0.5$, two bi-cellular and tetra-cellular flow structures were observed, which persist to be stable for all Rayleigh numbers examined. However, for the eccentricity $e\geqslant 0.5$, it was observed that the change between the two foregoing flow structures takes place at higher Rayleigh numbers, with inability to gain stable bi-cellular solution for Rayleigh numbers over the transition value. They mentioned that this behaviour is identical to that noticed by Barbosa Mota and Saatdjian (1994) for the concentric case with very small radius ratios. The results suggested that the thermal insulation is further effective when the eccentricity is set to the highest value in which a four-cell flow regime is generated rather than to the value that minimises the heat loss when the flow regime is bi-cellular. Barbosa Mota et al. (2000) also employed Darcy-Boussinesq's model to study natural convection in an elliptic annuli containing porous media utilising a high-order compact finite difference method. They found out that more horizontally flattening to the outer wall of the elliptic annulus changes unexpectedly the usual four-cellular flow pattern into the two-cellular flow pattern with co-rotating secondary cells. The later unusual flow regime is characterised owing to the fact that the secondary cell in each half-annulus is enfolded by the primary cell and is co-rotating, rather than is segregated from the primary cell and is counter-rotating as in the usual four-cellular flow regime. Also, interestingly, their numerical results showed that the flows in these two regimes are stable.

To the authors' knowledge, most of the works discussed above about natural convection in eccentric porous annuli concluded that the eccentricity effect does not cause the solutions losing stability, and they have been restricted to stable behaviours, which is obvious not the only case that can happen in actuality. In fact, instability is expected to occur in such physical problem due to mainly the reverse temperature gradient at the summit of the annulus, identical to the subject of the well-known *Bénard problem*. Indeed, all of these works above used the simple Darcy-Boussinesq's model with the thermal equilibrium assumption to calculate the flow and thermal fields.

The present study is to extend the previously published work by considering the full *Brinkman-Forchheimer-extended Darcy* (*BFD*) and the *Local Thermal non-Equilibrium* (*LTNE*) energy models for calculating the fluid velocity and temperatures, respectively. Indeed, this extension to the *BFD* and *LTNE* can be considered as a new feature in this study to investigate numerically natural convection inside eccentric annuli packed with spherical particles. In addition, effects of the annulus's eccentricity, in vertical, horizontal and diagonal directions, and the annulus's radius ratio, on the flow and the temperature distributions, and the rates of heat loss, as well as on the stability of the solutions, are investigated. Therefore, the another novelty in this work is the complicated geometry of three sorts of annuli considered, and this geometric parameter is included for different Rayleigh numbers.

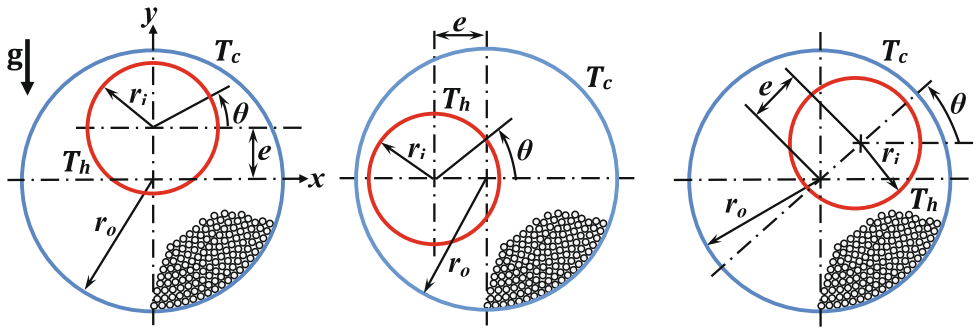

Fig. 1. Configurations of the eccentric annulus with coordinate system.

2. Problem statement

Fig. 1 displays the formulation of the problem considered. The system comprises of an eccentric horizontal annulus with an outer diameter D_o, an inner diameter D_i, and an annular space that has a radius ratio RR $= D_o/D_i$. The eccentricity e is identified as the distance between the centres of the inner and outer cylinders. The eccentricity is indicated as negative when the centre of the interior cylinder is below the centre of the exterior cylinder and vice versa. Vertical, horizontal, and diagonal eccentricities are taken into consideration. The annular cavity is filled with spherical particles saturated with air with Prandtl number Pr $=$ 0.71 and thermal conductivity $k_f = 0.02587$ W/m K at 20 °C. The packed bed of spheres are considered to be made from window glass characterised by a low porosity $\varepsilon = 0.5$ and a low thermal conductivity $k_s = 1.0$ W/m K at 20 °C. Hence, a constant solid/fluid thermal conductivity ratio $k_r = k_s/k_f = 1/0.02587 = 38.6$ is taken into account within this study. Also, the inner cylinder-to-particle diameter ratio is presumed to be fixed at $D_i/d = 30$. Initially at time $t = 0$, the external and internal annulus surfaces are assumed to be at the same temperature. However, at time $t > 0$, the internal surface is abruptly warmed up to T_h, and afterwards kept at that temperature with assuming that $T_h > T_c$. This swift alteration in the temperature establishes perspective unsteadiness in the system and producing a buoyancy-driven laminar flow.

3. Governing equations

The buoyancy-driven flow in the annular porous medium is supposed to be two-dimensional, unsteady, viscous, incompressible, and laminar. The fluid physical properties are assumed to be invariable, unless for the density involved in the buoyancy term of the y-momentum equation, which is permitted to change linearly with the temperature in accordance with the Boussinesq's approximation. The porous medium is presumed to be macroscopically isotropic and homogeneous. The *Brinkman-Forchheimer-extended* Darcy (*BFD*) model is used to calculate the fluid flow. Also, the hypothesis of the *Local Thermal non-Equilibrium* (*LTNE*) between the solid and fluid phases is assumed everywhere, so the two-equations energy model is employed to predict the temperatures of the two phases. Importantly, the governing equations in the porous bed are formulated on the basis of the fundamental principles of the volume averaging theorem Slattery (1967) and Whitaker (1967). Thereby, according to these assumptions, the mass, momentum and energy equations can have the following dimensional form (see, Vafai and Sozen (1994) and Amiri and Vafai (1994)):

$$\frac{\partial \dot{u}}{\partial \dot{x}} + \frac{\partial \dot{v}}{\partial \dot{y}} = 0, \tag{1}$$

$$\frac{\rho_f}{\varepsilon}\left(\frac{\partial \dot{u}}{\partial \dot{t}}\right) + \frac{\rho_f}{\varepsilon^2}\left(\dot{u}\frac{\partial \dot{u}}{\partial \dot{x}} + \dot{v}\frac{\partial \dot{u}}{\partial \dot{y}}\right) = -\frac{\partial \dot{p}}{\partial \dot{x}} + \frac{\mu_f}{\varepsilon}\left(\nabla^2 \dot{u}\right) + \dot{S}_u, \tag{2}$$

where,

$$\dot{S}_u = -\frac{\mu_f}{K}\dot{u} - \frac{\varepsilon.\rho_f C_F}{\sqrt{K}}\dot{|\mathbf{u}|}\dot{u}, \tag{3}$$

$$\frac{\rho_f}{\varepsilon}\left(\frac{\partial \dot{v}}{\partial \dot{t}}\right) + \frac{\rho_f}{\varepsilon^2}\left(\dot{u}\frac{\partial \dot{v}}{\partial \dot{x}} + \dot{v}\frac{\partial \dot{v}}{\partial \dot{y}}\right) = -\frac{\partial \dot{p}}{\partial \dot{y}} + \frac{\mu_f}{\varepsilon}\left(\nabla^2 \dot{v}\right) + \dot{S}_v + \rho_f \beta_f g\left(\dot{T} - \dot{T}_o\right), \tag{4}$$

where,

$$\dot{S}_v = -\frac{\mu_f}{K}\dot{v} - \frac{\varepsilon.\rho_f C_F}{\sqrt{K}}\dot{|\mathbf{u}|}\dot{v}, \tag{5}$$

here,

$$\dot{|\mathbf{u}|} = \sqrt{\dot{u}^2 + \dot{v}^2}, \tag{6}$$

$$\varepsilon\left(\rho c_p\right)_f\left(\frac{\partial \dot{T}_f}{\partial \dot{t}}\right) + \varepsilon\left(\rho c_p\right)_f\left(\dot{u}\frac{\partial \dot{T}_f}{\partial \dot{x}} + \dot{v}\frac{\partial \dot{T}_f}{\partial \dot{y}}\right) = \nabla\cdot\left(k_{f.\mathrm{eff}}\nabla \dot{T}_f\right) + h_{sf}a_{sf}\left(\dot{T}_s - \dot{T}_f\right), \tag{7}$$

$$(1-\varepsilon)\left(\rho c_p\right)_s\left(\frac{\partial \dot{T}_s}{\partial \dot{t}}\right) = \nabla\cdot\left(k_{s.\mathrm{eff}}\nabla \dot{T}_s\right) - h_{sf}a_{sf}\left(\dot{T}_s - \dot{T}_f\right), \tag{8}$$

where, $\dot{u}, \dot{v}$ are the dimensional horizontal and vertical velocity components along the dimensional $\dot{x}$ and $\dot{y}$ directions, and $\dot{T}$ and $\dot{p}$ are the dimensional temperature and pressure. The subscripts f and s denote the mobile fluid phase and the stationary solid phase, respectively, and eff and ε refer to the effective property and the porosity, respectively. While, $\dot{S}_u$ and $\dot{S}_v$ are the dimensional source terms in the momentum equations. In order to analyse the flow and thermal fields in general scale, the following scaling parameters are selected as D_i, the diameter of the inner cylinder, α_f, the fluid thermal diffusivity, $(T_h - T_c)$, the temperature difference between the hot inner and the cold outer cylinders, and $\rho_f\alpha_f^2$, the characteristic pressure, and the non-dimensional variables are defined as:

$$x, y = \frac{\dot{x}, \dot{y}}{D_i}, \quad u, v = \frac{\dot{u}, \dot{v}\, D_i}{\alpha_f}, \quad T_{f,s} = \frac{(\dot{T}_{f,s} - T_c)}{(T_h - T_c)}, \quad P = \frac{\dot{p}\, D_i^2}{\rho_f \alpha_f^2}. \tag{9}$$

With the substitution of these variables in the aforementioned governing conservation equations (1–8), the following non-dimensional equations are obtained:

$$\frac{\partial u}{\partial x} + \frac{\partial v}{\partial y} = 0, \tag{10}$$

$$\left(\frac{\partial u}{\partial t}\right)+\frac{1}{\varepsilon}\left(u\frac{\partial u}{\partial x}+v\frac{\partial u}{\partial y}\right)=-\varepsilon\left(\frac{\partial p}{\partial x}\right)+Pr\left(\nabla^2 u\right)+S_u, \tag{11}$$

where,

$$S_u=-\frac{\varepsilon Pr}{Da}u-\frac{\varepsilon^2.C_F}{\sqrt{Da}}|\vec{\mathbf{u}}|u, \tag{12}$$

$$\left(\frac{\partial v}{\partial t}\right)+\frac{1}{\varepsilon}\left(v\frac{\partial v}{\partial x}+v\frac{\partial v}{\partial y}\right)=-\varepsilon\left(\frac{\partial p}{\partial y}\right)+Pr\left(\nabla^2 v\right)+S_v+\varepsilon RaPrT_f, \tag{13}$$

where,

$$S_v=-\frac{\varepsilon Pr}{Da}v-\frac{\varepsilon^2.C_F}{\sqrt{Da}}|\vec{\mathbf{u}}|v, \tag{14}$$

and,

$$|\vec{\mathbf{u}}|=\sqrt{u^2+v^2}, \tag{15}$$

$$\left(\frac{\partial T_f}{\partial t}\right)+\left(u\frac{\partial T_f}{\partial x}+v\frac{\partial T_f}{\partial y}\right)=\nabla\cdot\left(\frac{k_{f.\mathrm{eff}}}{k_f}\nabla T_f\right)+\frac{Bik_r}{\varepsilon}\left(T_s-T_f\right), \tag{16}$$

$$\left(\frac{\partial T_s}{\partial t}\right)=\nabla\cdot\left(\frac{k_{s.\mathrm{eff}}}{k_s}\nabla T_s\right)-\frac{Bi\alpha_r}{(1-\varepsilon)}\left(T_s-T_f\right). \tag{17}$$

The fluid and solid effective thermal conductivity $k_{f.\mathrm{eff}}$ and $k_{s.\mathrm{eff}}$, respectively, in the diffusion terms of Eqs. 16 and 17 represent the stagnant conductivity of the two phases, which can be calculated based on the experimental correlation of Zehner and Schluender (1970) as follows:

$$\frac{k_{f.\mathrm{eff}}}{k_f}=\left(1-\sqrt{1-\varepsilon}\right)+\left(\frac{2\sqrt{1-\varepsilon}}{1-\lambda B}\right)\left(\frac{(1-\lambda)B}{(1-\lambda B)^2}\ln(\lambda B)-\frac{B+1}{2}-\frac{B-1}{1-\lambda B}\right), \tag{18}$$

$$\frac{k_{s.\mathrm{eff}}}{k_s}=(1-\varepsilon), \tag{19}$$

where $\lambda=1/k_r$ and $B=1.25((1-\varepsilon)/\varepsilon)^{\frac{10}{9}}$. The main dimensionless parameters of the problem emerging in equations (10–17) are Rayleigh, Darcy, and Biot numbers, based on the inner cylinder diameter. They are denoted respectively by:

$$Ra=\frac{g\beta_f D_i^3(T_h-T_c)}{\alpha_f\nu_f},\quad Da=\frac{K}{D_i^2},\quad Bi=\frac{D_i^2 h_{sf}a_{sf}}{k_s}, \tag{20}$$

where, ν_f and α_f are the fluid kinematic viscosity and the thermal diffusivity, respectively, and β_f and g are the volumetric expansion coefficient and the gravitational acceleration, respectively. In addition, K and C_F are the permeability and the inertia coefficient, respectively, of the spherical particles, which are calculated according to the Ergun's empirical expressions Ergun (1952) based on the particle diameter d and the porosity ε as follows:

$$K=\frac{\varepsilon^3 d^2}{150(1-\varepsilon)^2}, \tag{21}$$

$$C_F=\frac{1.75}{\sqrt{150\varepsilon^3}}, \tag{22}$$

whereas, a_{sf} represents the specific surface area of the solid particles, while h_{sf} represents the particle-to-fluid convective heat transfer coefficient in the porous bed. The expression of Dullien (1979) for calculating a_{sf}, and the correlation of Wakao et al. (1979) for calculating h_{sf}, are employed as follows:

$$a_{sf}=\frac{6(1-\varepsilon)}{d}, \tag{23}$$

$$h_{sf}=\frac{k_f}{d}\left(2+(Pr)^{1/3}\left(Re_p\right)^{0.6}\right), \tag{24}$$

where, Re_p is the Reynolds number in the particle level,

$$Re_p=\frac{|\vec{\mathbf{u}}|d}{\nu_f}. \tag{25}$$

Therefore, from Eqs. (20)–(24), the Darcy and Biot numbers can be expressed as functions of the porosity ε, the inner cylinder-to-particle diameter ratio D_i/d, and the solid/fluid thermal conductivity ratio k_r as follows:

$$Da=\left(\frac{d}{D_i}\right)^2\frac{\varepsilon^3}{150(1-\varepsilon)^2}, \tag{26}$$

$$Bi=6(1-\varepsilon)\left(\frac{1}{k_r}\right)\left(\frac{D_i}{d}\right)^2\left(2+(Pr)^{1/3}\left(Re_p\right)^{0.6}\right). \tag{27}$$

4. Boundary conditions

The motion of the flowing air is demonstrated utilising the stream function Ψ gained from the calculated velocity components u and v by: $u=\partial\Psi/\partial y$ and $v=-\partial\Psi/\partial x$. The velocity components are assumed $u=v=0$ on all solid boundaries of the cylinders. While, the boundary conditions for the dimensionless temperatures are assumed as follows:

$$\begin{aligned} T_f=T_s=1 \quad &\text{at} \quad (r=r_i) \quad \text{and} \quad (0<\theta^o<360),\\ T_f=T_s=0 \quad &\text{at} \quad (r=r_o) \quad \text{and} \quad (0<\theta^o<360). \end{aligned} \tag{28}$$

The heat transfer rates across the fluid and solid phases represent the physical entity of concern in this study and are calculated by applying the Fourier's law at the heated inner cylinder surface as follows:

$$q_f=-\frac{k_{f.\mathrm{eff}}}{k_f}\frac{\partial T_f'}{\partial n}|_{r=r_i},\quad q_s=-\frac{k_{s.\mathrm{eff}}}{k_s}\frac{\partial T_s'}{\partial n}|_{r=r_i}, \tag{29}$$

and in terms of the non-dimensional parameters,

$$\begin{aligned} Nu_f&=\frac{q_f D_i}{(T_h-T_f')}=\frac{1}{S}\int_0^S\frac{k_{f.\mathrm{eff}}}{k_f}\frac{\partial\theta_f}{\partial\mathbf{n}}d\mathbf{s}|_{r=r_i},\\ Nu_s&=\frac{q_s D_i}{(T_h-T_s')}=\frac{1}{S}\int_0^S\frac{k_{s.\mathrm{eff}}}{k_s}\frac{\partial T_s}{\partial\mathbf{n}}d\mathbf{s}|_{r=r_i}, \end{aligned} \tag{30}$$

where, Nu^f and Nu^s refer to the fluid and solid Nusselt numbers, respectively, $\mathbf{n}$ and $\mathbf{t}$ refer to the perpendicular and tangential directions at the inner cylinder wall, respectively, and S refers to the periphery of the inner cylinder. Also, the total Nusselt number Nu_t can be calculated as the summation of Nu^f and Nu^s:

$$Nu_t=Nu_f+Nu_s. \tag{31}$$

5. Computational procedure

The time-split spectral element method, explained thoroughly in Karniadakis et al. (1991) and Thompson et al. (2006), is used to numerically solve the above non-dimensional governing Eqs. (10)–(17) for analysing the transient momentum and energy transport in the unsteady natural convection regime. This approach is incorporated in our existing in–house code to discretise the equations in time as well as the space. In the temporal discretisation, an "explicit approach" (Adams–Bashforth) is used to deal with the advection term due to the nature of non-linearity, whereas an "implicit approach" (Adams–Moulton) is employed for handling the pressure and diffusion terms. This discretisation method is extensively described in Chorin

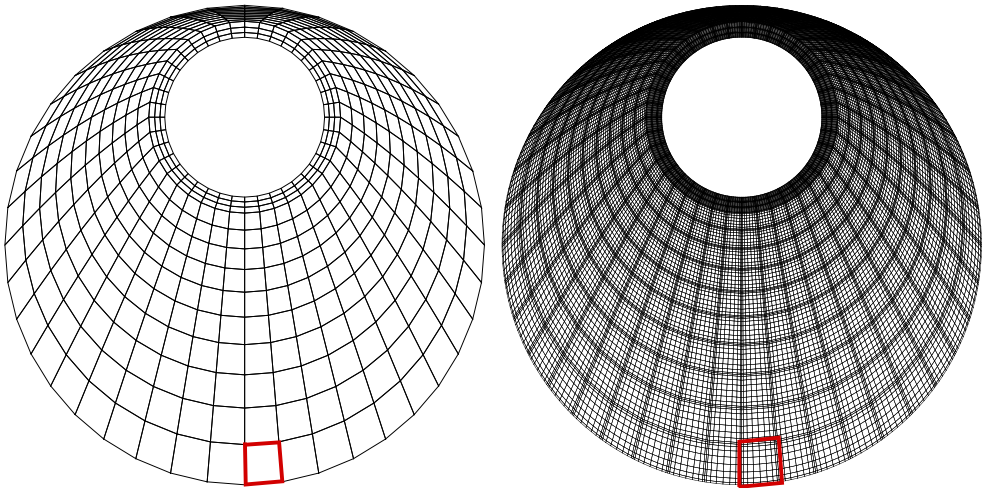

Fig. 2. (Left) Typical macro-elements. (Right) Elements are further subdivided into (9 × 9) internal node points.

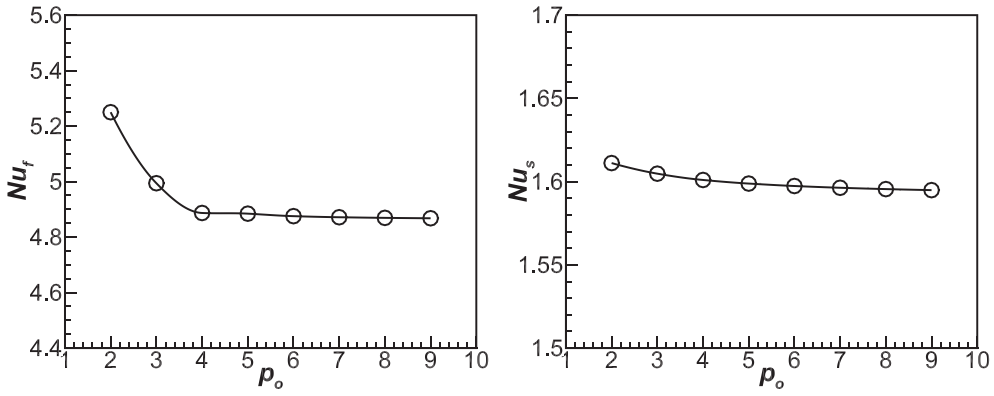

Fig. 3. Nusselt number within (Left) fluid phase and (Right) solid phase, with polynomial degree p_o, for the mesh resolution study.

(1968), Karniadakis et al. (1991) and Thompson et al. (2006). While, the Galerkin technique, reported by Fletcher (1984), Fletcher (1991) and Karniadakis and Sherwin (2005), of the nodal-based spectral-element is used for discretising the equations in space. Thus, the computational domain is divided into a group of coarse quadrilateral macro-elements. A refinement that is called a (*h*-refinement) for the macro-mesh generated can be made in zones that experience high gradients such as close to solid boundaries. Also, the macro-elements employ high-order Lagrange polynomials depending on Gauss–Lobatto-Legendre quadrature points as weighting and shape functions within the integration process of the equations. Using non-linear high-order polynomials permits each macro-element to be subdivided further into ($N_x \times N_y$) nodes towards more enhancement (*p*-refinement) in the mesh resolution. Thereby, in this ($h-p$) discretisation approach, the computational area is discretised just once with as much as exemplary macro-element mesh, and afterwards a precise solution can be acquired by only increasing the polynomial order (*po*) at the run time before the numerical convergence is accomplished.

The present study employs a typical computational mesh, which is comprised of 520 macro-elements and 560 nodes, and is illustrated in Fig. 2(Left). Later, a grid resolution study is performed for the configuration shown in Fig. 2(Left) by changing the Lagrangian polynomial, *po* = 2–9, to guarantee that the current obtained results are unrelated to the spatial mesh size. Many numerical simulations were conducted at various values of eccentricity and Rayleigh number, and the average fluid and solid Nusselt numbers Nu^f and Nu^s were monitored as accuracy indication. For brevity, sample of the results are demonstrated in Fig. 3 for the case of vertical eccentric annulus at Rayleigh number Ra = 5×10^7 and eccentricity $e = 0.8$. The results shown in Fig. 3 depict that Nu_f and Nu_s are converged by $po = 8$ with relative errors of lower than 0.1%. This results in a group of (9 × 9) internal node points throughout each macro-element of the grid, whereas keeping the same structure of the macro-element. Fig. 2(Right) shows the spectral micro-elements computational grid employed in the present simulations.

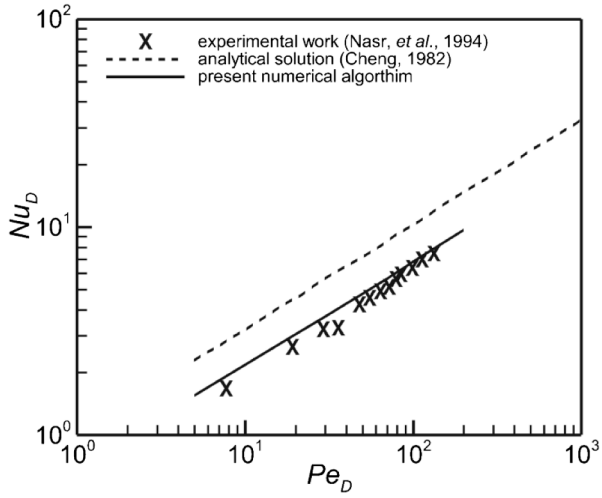

Fig. 4. Comparison between our numerical results with experimental and analytical results of Nasr et al. (1994) and Cheng (1982).

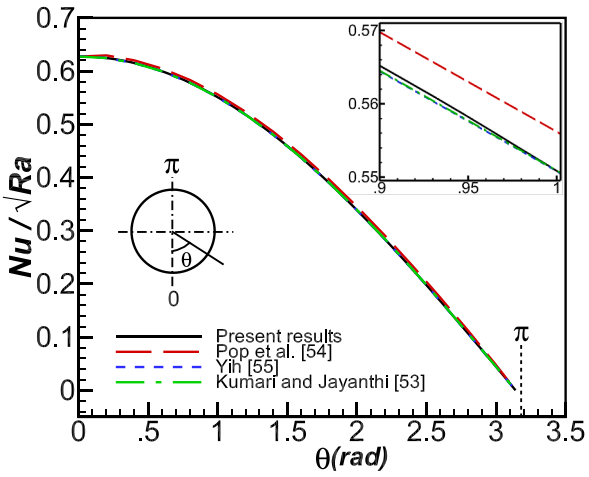

Fig. 5. Comparison for angular local Nusselt number $Nu/\sqrt{Ra}$ along the cylinder circumference between the results of the present code with the results of Pop et al. (1992), Yih (1999) and Kumari and Jayanthi (2004).

The current algorithm was previously verified for related problems such as forced convection from a single cylinder by Al-Sumaily et al. (2012) and Al-Sumaily and Thompson (2013) and from multi-cylinders by Al-Sumaily (2014), as well as for natural convection from a single cylinder by Al-Sumaily (2014), embedded in a packed bed of spheres. Additional verifications for the implementation of the current algorithm were performed. Thus, results from our code were compared with the analytical and the experimental results formerly published by Cheng (1982) and Nasr et al. (1994), respectively, for convection heat transfer from a cylinder of diameter $D = 2.7$ mm, and immersed in a packed bed of spherical aluminium. particles with $d_p = 12.23\ mm$. The comparison, which is displayed in Fig. 4 for the variation of average Nusselt number against Péclet number Pe_D, shows obviously an acceptable agreement between the present numerical results and the two analytical and experimental results. Furthermore, the accuracy of the present code was also checked by comparing its results with these of Kumari and Jayanthi (2004), Pop et al. (1992) and Yih (1999), for the problem of free convection heat transfer from a circular cylinder situated inside a saturated porous medium in the condition of thermal equilibrium. Fig. 5 depicts this comparison, and demonstrates a good agreement for our code with a maximum deviation less than 0.05%.

6. Results and discussion

The numerical results are obtained by considering Prandtl number $Pr = 0.7$ for air as a flowing fluid. Whereas, the porous medium is a packed bed of spherical particles made of window-glass as a thermal insulator with a porosity corresponding to $\varepsilon = 0.5$ and solid-to-fluid thermal conductivity $k_r = 38.6$. The particles that are packed inside the cylindrical gap between the two cylinder have size kept constant with inner cylinder-to-particle diameter ratio $D_i/d = 30$. The focus is on the geometrical parameters, which are the annulus's eccentricity ($-0.8 \leqslant e \leqslant 0.8$) in three vertical, horizontal, and diagonal directions and the radius ratio ($1.5 \leqslant RR \leqslant 5.0$), in order to analyse the velocity and temperature fields as well as the local heat transfer on the cylindrical surface before calculating the overall heat transfer throughout both the fluid and solid phases, to including results for a wide range of Rayleigh number ($10^4 \leqslant Ra \leqslant 8 \times 10^7$). Thus, searching for a perfect configuration resulting to a maximum reduction in heat transfer is the first priority in the present study. Also, in order to investigate the instabilities that can take place in the fluid motion for given geometrical parameters and Rayleigh numbers.

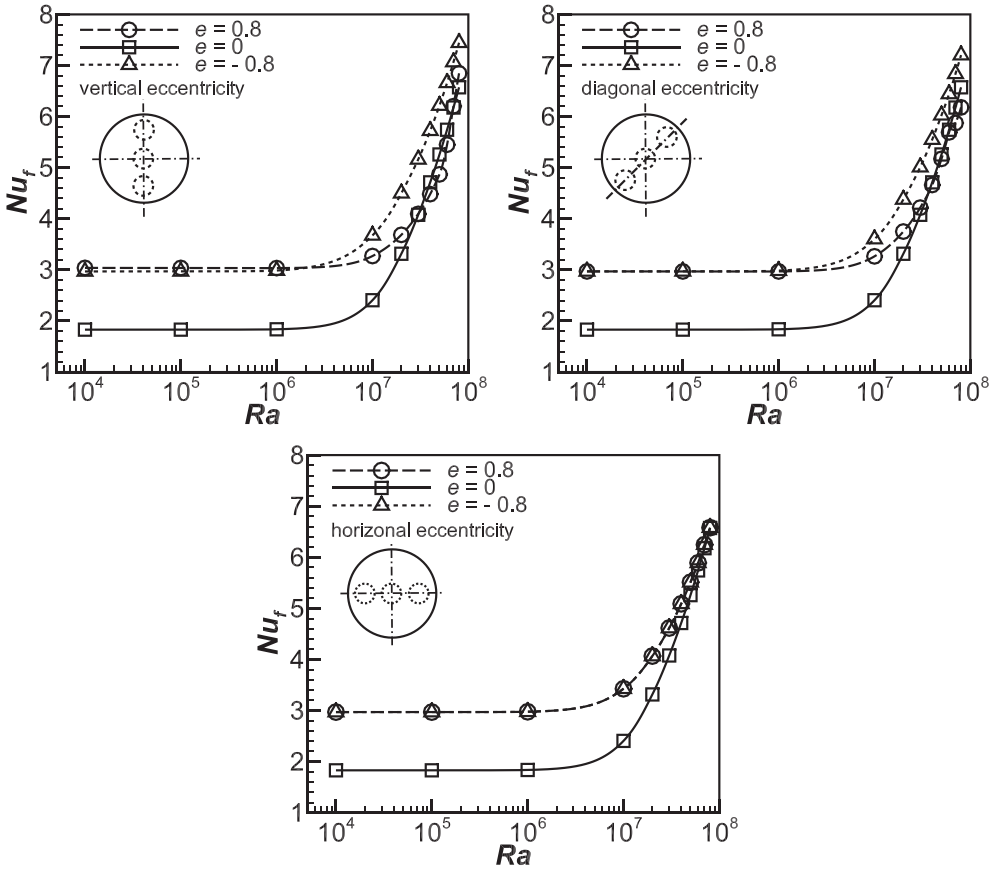

Fig. 6. Fluid mean Nusselt number Nu^f with Ra for radius ratio of RR = 2, at different vertical, diagonal, and horizontal eccentricities $e = -0.8, 0, 0.8$.

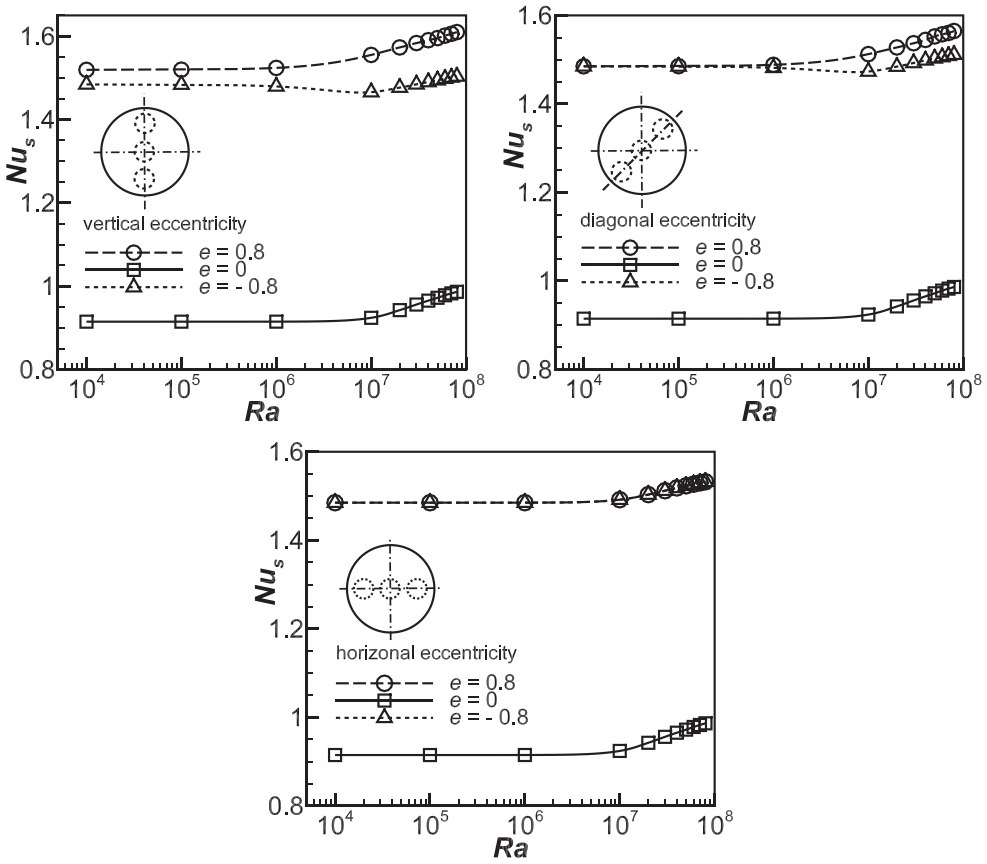

Fig. 7. Solid mean Nusselt number Nu^s with Ra for radius ratio RR = 2, at different vertical, diagonal, and horizontal eccentricities $e = -0.8$, 0, 0.8.

The variation of the average heat transfer from the inner cylinder represented by Nusselt number throughout the fluid phase (Nu^f) and the solid phase (Nu^s) with Rayleigh number are shown in Figs. 6 and 7, respectively, for vertical, diagonal, and horizontal eccentricities $e = -0.8$, 0, 0.8, using a fixed radius ratio RR = 2. In Fig. 6, it can be seen that for the three vertical, diagonal, and horizontal eccentric configurations considered here, the extreme negative and positive eccentricities $e = -0.8$ and 0.8, respectively, seem to be much better for heat transfer enhancement than the concentric situation when $e = 0$, for low and moderate Rayleigh numbers, $Ra \leqslant 10^7$, with no influence from Rayleigh number. However, as Rayleigh number increases behind 10^7, Nu^f increases significantly with Rayleigh number, and Nu^f for the vertical and diagonal configurations at $e = -0.8$ is higher than that at other eccentricities $e = 0$ and 0.8. Also, Nu^f for these configurations is greater than that for the horizontal one at $e = -0.8$ and 0.8. It is shown that the horizontal situation gives similar converged heat transfer performance at all eccentricities $e = -0.8$, 0, 0.8 for very high Rayleigh number. However, Fig. 7 shows that the variation of Nu^s is approximately flat and robustly independent on Rayleigh number. Also, the values of Nu^s for the concentric annulus at $e = 0$ and the positive eccentric annulus at $e = 0.8$ are higher than those for the negative eccentric annulus at $e = -0.8$. This is true when moving the inner cylinder in the three vertically, horizontally, and diagonally directions. In addition, it can be seen that the rates of Nu^s are lower than those of Nu^f in Fig. 6, by roughly between 2.5–6.5 times for the concentric annulus and by nearly between 2–4.5 for the positive and negative eccentric annuli for Rayleigh number between $Ra = 10^4 - 8 \times 10^7$.

The impact of Rayleigh number on the hydrodynamic and thermal fields in the vertical, diagonal, and horizontal eccentric configurations are shown in Figs. 8–10, respectively, at two eccentricities $e = -0.8$ (negative location) and 0.8 (positive location) (Note that the red colour refers to high temperatures and the blue colour for low temperatures). In Fig. 8, when the inner cylinder is located downstream at $e = -0.8$, an expected flow regime is obtained, thus, it is characterised by a main primary cell in each half-annulus forming which is called a uni-cellular flow regime. In this regime, it is seen that the fluid close the interior cylinder ascends over its periphery and the boundary layer separates from the top surface at ($\theta = 90°$). As time goes on further, the split fluid at the top surface ascends structuring an upward flow that hits the top surface of the annulus and descends along the outer perimeter constructing a downward flow. Both of these two upward and downward flows form the primary rotating eddy in each half-annulus. It is seen that by increasing Rayleigh number, the intensity of the uni-cellular flow and the thermal convection in the annular gap increase producing an interesting thermal plume behaviour.

Moving the inner cylinder vertically upwards to the extreme positive position $e = 0.8$, decreases the gap spacing in the upper area of the annulus, and as a result reducing the influence of crescent-shaped convection and increasing the impact of the conduction heat transfer. However, the increment in Rayleigh number causes the convection effect in this zone to become stronger again.

Thus, Fig. 8b demonstrates that at $Ra = 5 \times 10^7$, the flow in the upper layer differs slightly from the usual uni-cellular flow pattern at $Ra < 5 \times 10^7$, where there is seen a secondary cell in every half-annulus enfolded by the primary cell and is co-rotating. While, as Rayleigh number increases to $Ra = 6 \times 10^7$, the secondary cell is shown to segregate from the primary cell and is counter-rotating, forming which is called a bi-cellular flow regime. The segregation of the secondary cell is due to the constitution of a stagnant zone in the top region, consequently, the flow boundary layer at the interior cylinder is split from its surface at a position ($\theta \neq 90°$), and a little counter-rotating eddy connected to the cylinder is generated. By increasing Rayleigh number to $Ra = 7 \times 10^7$, a

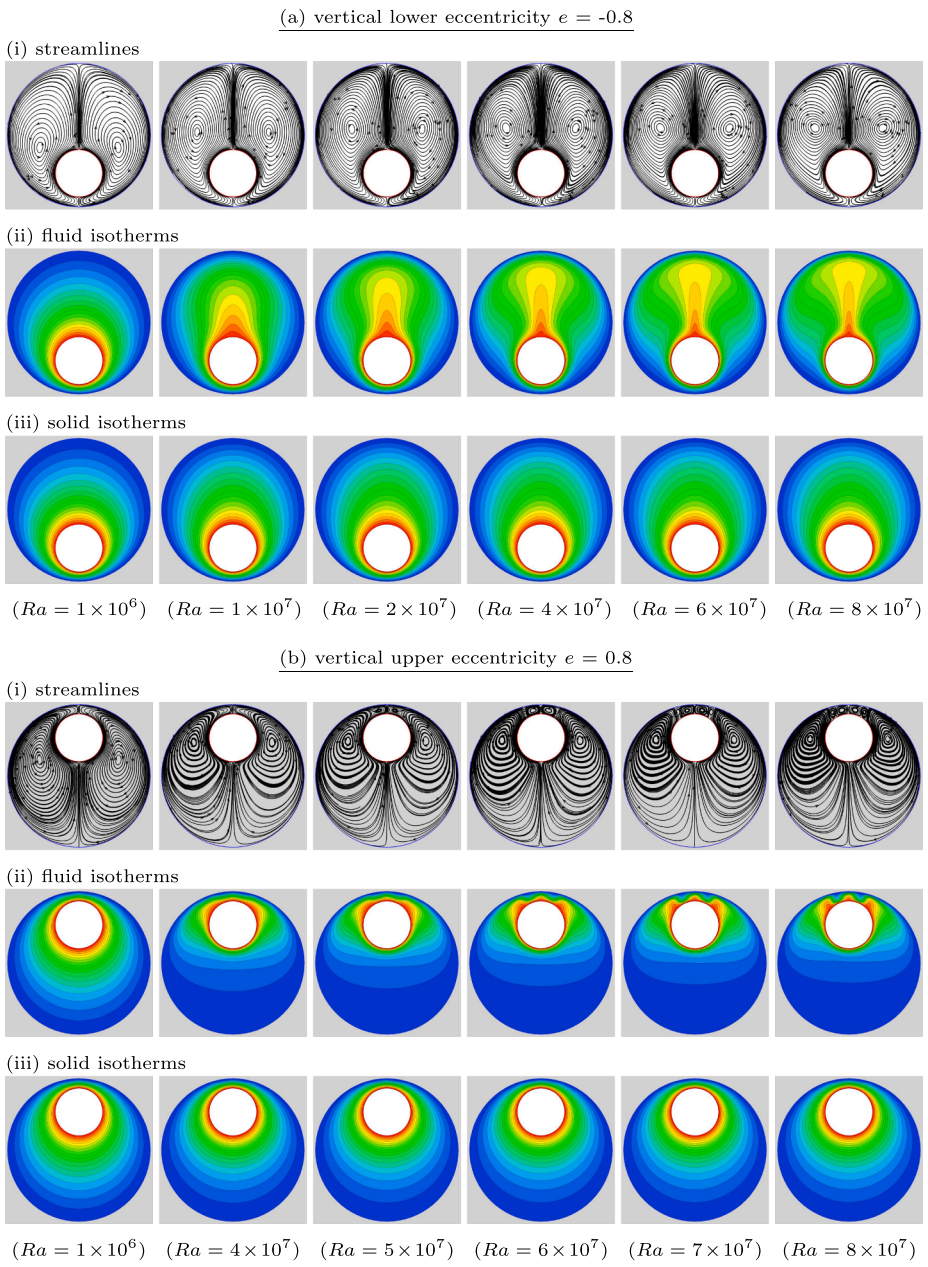

Fig. 8. Patterns of (i) streamlines, (ii) fluid isotherms, and (iii) solid isotherms, for lower negative and upper positive vertical eccentricities (a) $e = -0.8$ and (b) $e = 0.8$, for radius ratio RR = 2, at different Ra.

tri-cellular or multi-cellular flow is obtained, which becomes more clear at Ra $= 8 \times 10^7$.

Fig. 9 illustrates the flow and thermal fields for the two diagonal eccentricities $e = -0.8$ at the bottom left and $e = 0.8$ at the top right. The results obtained for the case of lower negative eccentricity $e = -0.8$ show that the uni-cellular flow still remains and prevails in the annulus layer. One can see that as Rayleigh number increases, the convective phenomena becomes more important, and the extent of the right kidney-shaped vortex increases. While, when the inner cylinder is positioned at the extreme upper right of the annulus (upper positive eccentricity) $e = 0.8$, the streamlines of the multi-cellular flow regimes, which occur on the combined effect of convection and conduction, are shown to be deformed and the isotherms are particularly distorted when the Rayleigh number increases after Ra $= 4 \times 10^7$. Fig. 10 demonstrates the flow and thermal fields when the interior cylinder is located horizontally to the maximum left and right. The results show that the extent of left and right kidney-shaped eddies gradually grows as the gap enlarges, and the centre of the circulating flow moves upward in the annulus. Generally, for this case whatever the Rayleigh number is, a symmetric uni-cellular flow with respect to the vertical axis, is seen.

Fig. 11 depicts the evolution of the average fluid Nusselt number Nu_f calculated on the inner cylinder as function of time for the vertical and diagonal eccentric configurations, at three closer locations $e = 0.4$, 0.6, 0.8, and at different values of Rayleigh number. From the figure, one can remark that in the vertical eccentric configuration, Nu_f does not oscillate in time, and the curves of Nu_f converge to the stable condition for all values of eccentricity and Rayleigh number, except interestingly at two certain cases. The circumstances of the first case are when Rayleigh number equals to Ra $= 7 \times 10^7$ and the eccentricity at $e = 0.8$, while the conditions of the second case are when Ra $= 5 \times 10^7$ and the eccentricity at $e = 0.6$. In the first case, the oscillation seems to have regular downward shape pulses every roughly 2 units time. However, in the second case, it is shown that the time signal differs significantly from

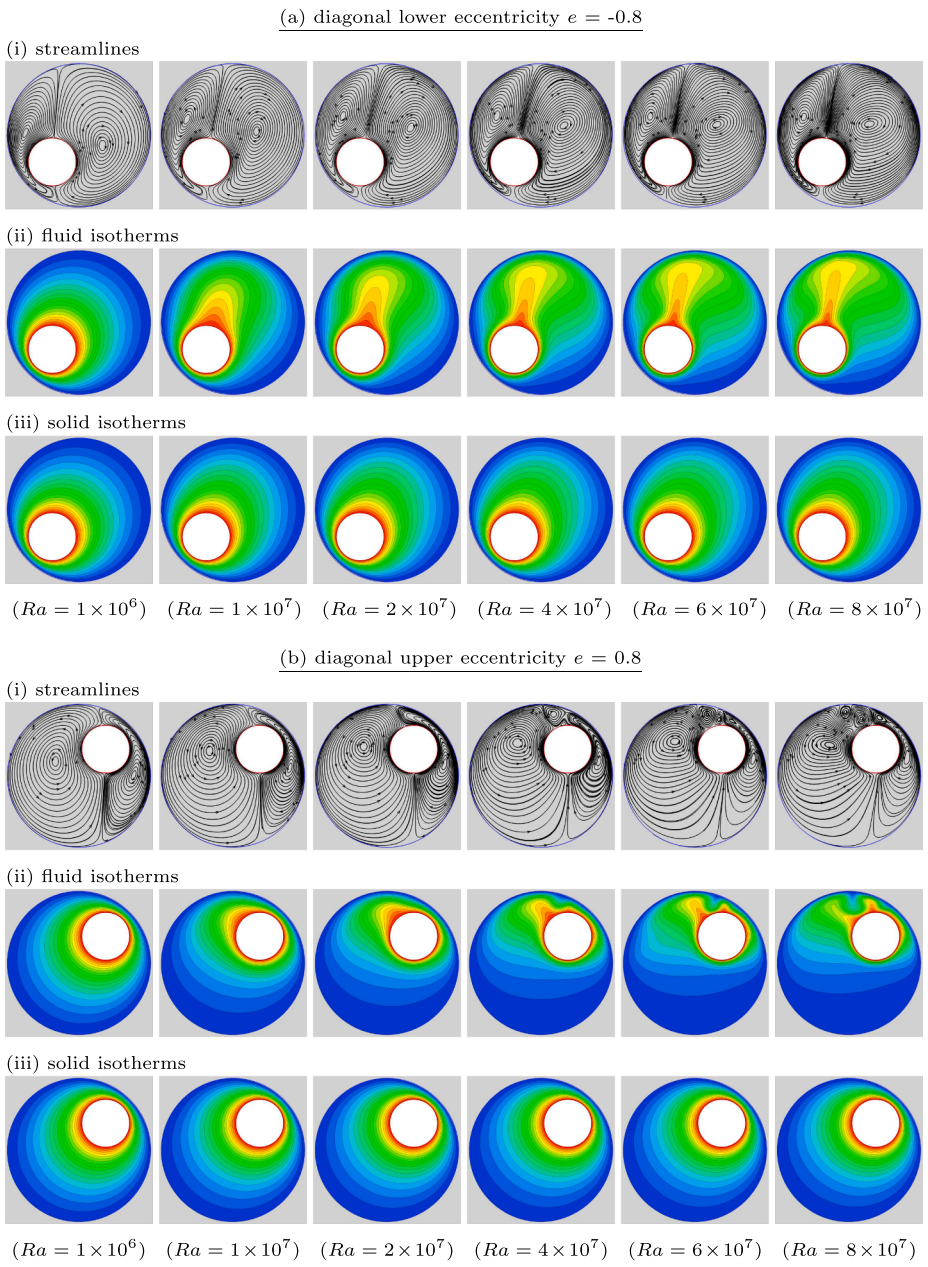

Fig. 9. Patterns of (i) streamlines, (ii) fluid isotherms, and (ii) solid isotherms, for lower negative and upper positive diagonal eccentricities (a) $e = -0.8$ and (b) $e = 0.8$, for radius ratio RR = 2, at different Ra.

that in the first case, where Nu^f is oscillating with time in a fully periodic regime.

In the other hand, in the diagonal eccentric configuration, we conclude that the fluid flow loses drastically its stability at the closest location $e = 0.8$ for moderate and higher Rayleigh numbers $Ra \geqslant 4 \times 10^7$. The curves of Nu^f at $e = 0.8$ suggest that as Rayleigh number increases, the transition from a steady to a fully unsteady periodic behaviour happens faster. Whereas, the fluid flow gains the stability as Rayleigh number decreases below 4×10^7, as well as when the eccentricity decreases under $e = 0.8$ for all Rayleigh numbers, except extraordinarily at $Ra = 4$ and 5×10^7, when $e = 0.6$. The time history of Nu^f for these two exceptional cases shows a new instability with similar behaviour of periodicity. The shape of this periodicity is regular pulsatile with plateaus produced every one unit time, with high-frequency oscillations for higher Rayleigh number. In General, this unstable behaviours aforementioned in the vertical and diagonal configurations represent which are called *Rayleigh-Bénard* thermal instabilities occur in the top region of the porous layer, which stimulate big temperature gradients on the interior cylinder and could be unfavourable for purposes of thermal insulation. The results also show that the flow behaviour in the horizontal eccentric geometry is stable for all eccentricities and Rayleigh numbers.

Some details of the unsteady convective flows are displayed in Figs. 12–14 for three cases at different indicated times when Nu^f reaches maximum and minimum values. The first case is for a vertical eccentric geometry at $e = 0.8$ and $Ra = 7 \times 10^7$, and the other two cases are for a diagonal eccentric geometry at $e = 0.8$ with $Ra = 8 \times 10^7$ and at $e = 0.6$ with $Ra = 5 \times 10^7$, respectively. The first instability demonstrated in Fig. 12 produces a large change in the dynamics of the system, which shows a transition from a tri-cellular flow at t_1 to a bi-cellular flow at t_3, and then to uni-cellular at t_4, and vice versa throughout t_4, t_5, and t_6. Fig. 13 shows the flow dynamic of the fully periodic flow over a full one

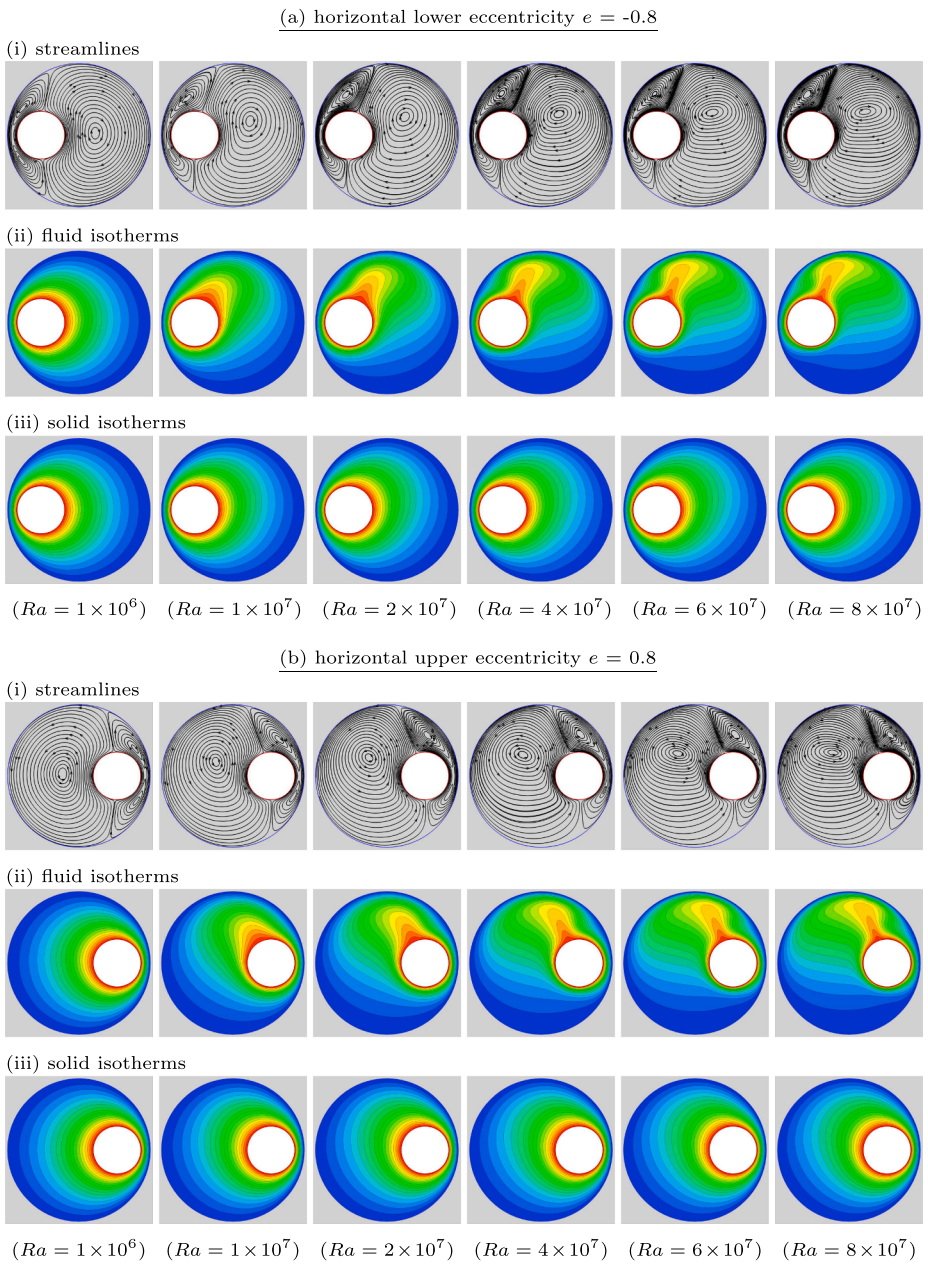

Fig. 10. Patterns of (i) streamlines, (ii) fluid isotherms, and (ii) solid isotherms, for lower negative and upper positive horizontal eccentricities (a) $e = -0.8$ and (b) $e = 0.8$, for radius ratio RR = 2, at different Ra.

period of time. It is shown that the maximum Nu^f occurs in the flow with multi cells formed above the inner cylinder. While, observations in Fig. 14 show the flow behaviour over a complete plateau of a higher oscillation frequency. The multi-cellular flow seems to flap horizontally above the inner cylinder.

The attention is now turned to display the effect of developing secondary cells in the top layer of annulus as Rayleigh number increments on the evolution of the local Nusselt number Nu_{Lf} along the inner cylinder surface. The variation of Nu_{Lf} curves at the highest positive vertical and diagonal eccentricities $e = 0.8$ are depicted in Fig. 15 at different Rayleigh numbers. In the vertical eccentric annulus, before the presence of secondary cells, the upsurge is greater at an angle $\theta = 270^\circ$ for which the rise in the fluid temperature gradient behind the interior cylinder induce higher local heat transfer. The influences of the two secondary cells generated in the left region of annulus around the angle $\theta = 75^\circ$ and the another two secondary cells produced in the right region around around the angle $\theta = 105^\circ$ become more significant as Rayleigh number increases. However, as the inner cylinder moves clockwise by $\theta = 45^\circ$ (in diagonal eccentric annulus), the vertical movement of the buoyancy forces deforms the secondary eddies generated, and a decay in the disturbed local heat dissipation is shown upstream of the annulus tracked by an upturn downstream.

In prior Fig. 6, it was observed that for low Rayleigh numbers, the fluid mean Nusselt number Nu^f may be further maximised if the concentric annulus that generates the minimum heat dissipation is constructed eccentric. However, for high Rayleigh numbers, the one can presume that an optimum eccentricity value exists in which the heat dissipation is minimised. The results that are presented in Figs. 16–18 depict the variation of Nu^f against the eccentricity, $(-0.8 \leqslant e \leqslant 0.8)$ nine values in step of 0.02. in vertical, diagonal, and horizontal directions, respectively, employing a fixed radius ratio RR = 2. It is shown that in all these three cases, for low Rayleigh numbers, i.e. $Ra \leqslant 1 \times 10^6$, the minimum Nu^f is situated at $e = 0$, pointing out that the concentric configuration is the best effectual one for the thermal insulation. While,

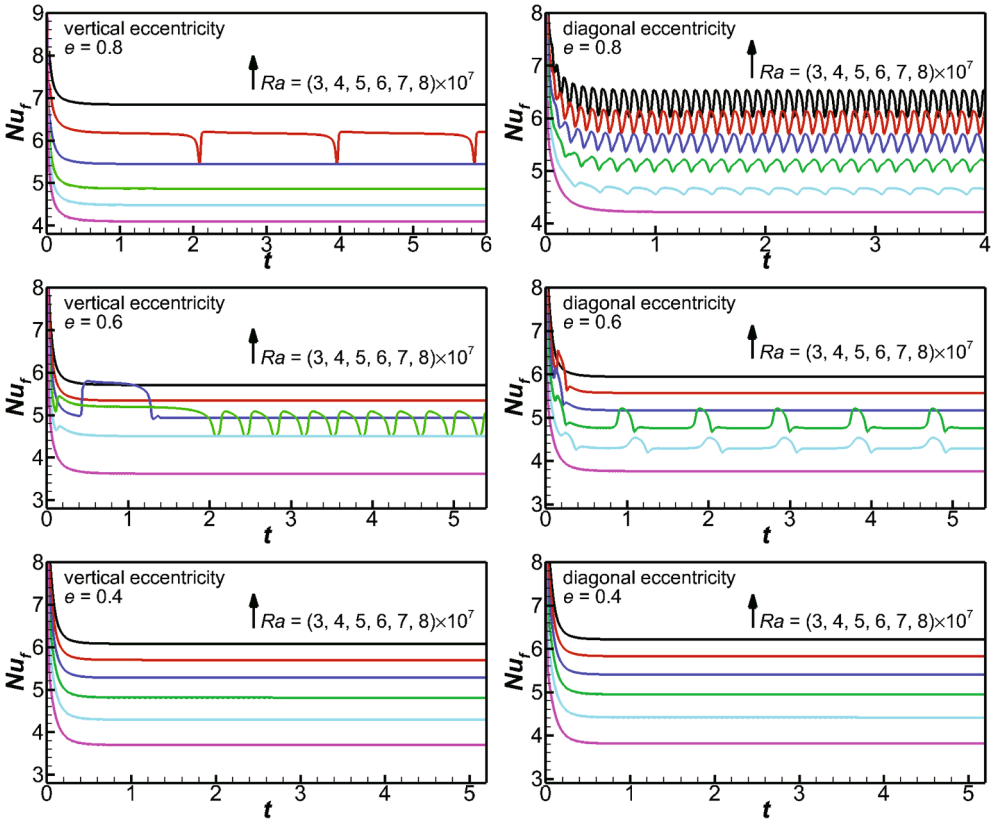

Fig. 11. Time evolution of Nu^f for (Left) vertical eccentricity and (Right) diagonal eccentricity, at $e = 0.8, 0.6, 0.4$, with increasing values of Ra.

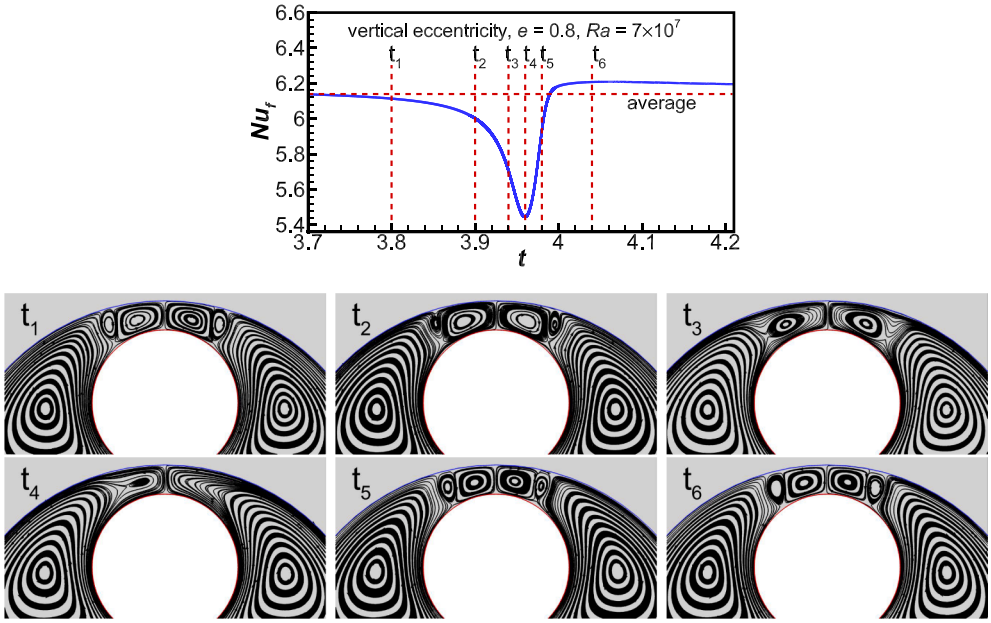

Fig. 12. Details of flow behaviour for the case of vertical eccentricity at $e = 0.8$ and $Ra = 7\times10^7$ shown in Fig. 12, over one periodic pulse at the times indicated by red circular points.

a steep increase in Nu^f is found to be at larger negative and positive values of eccentricity, which is coincident with the expansion of gap thickness in the top or bottom parts, respectively, of the annulus. However, as Rayleigh number increases, the eccentricity influence in the vertical and diagonal geometries is significantly different from that in the horizontal one. Thus, the value of the eccentricity that locates the minimum Nu^f increases with Rayleigh number, until reaching an optimal value of eccentricity at $e = 0.6$, which can be considered as a better effectively eccentric insulation than concentric one. For larger positive value of $e = 0.8$ where the top layer becomes so slender, Nu^f leaps suddenly due to the effect of cold wall of the outer cylinder. This jump in Nu^f is more significant at higher $Ra \geqslant 4 \times 10^7$ as a result of a better efficacious fluid mixing owing to the supplementary counter-rotating cells. Thus, the emergence of the co-rotating cell and the

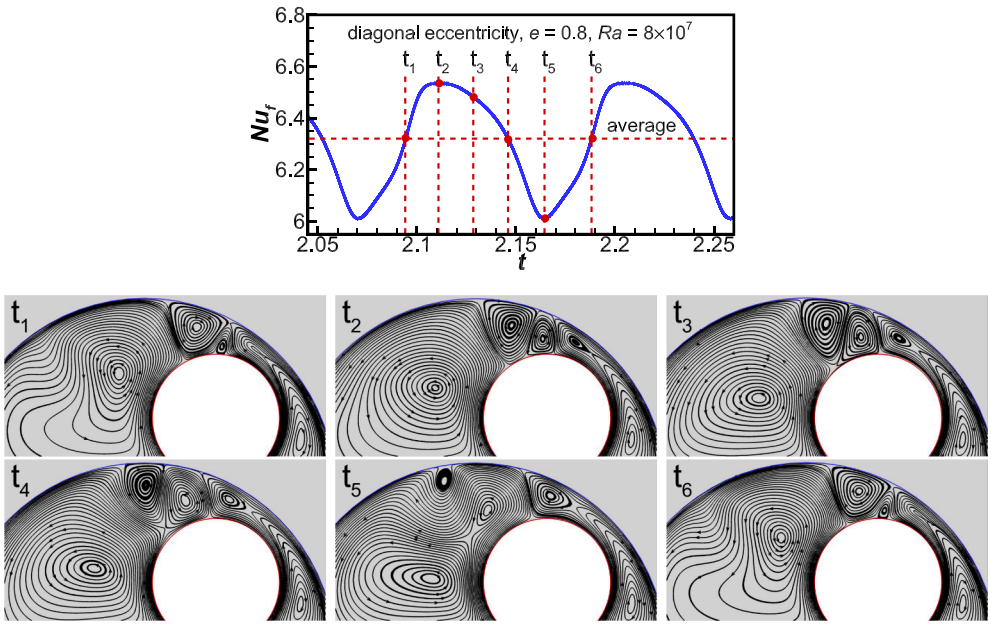

Fig. 13. Details of flow behaviour for the case of diagonal eccentricity at $e = 0.8$ and Ra $= 8\times10^7$ shown in Fig. 12, over one period at the times indicated by red circular points.

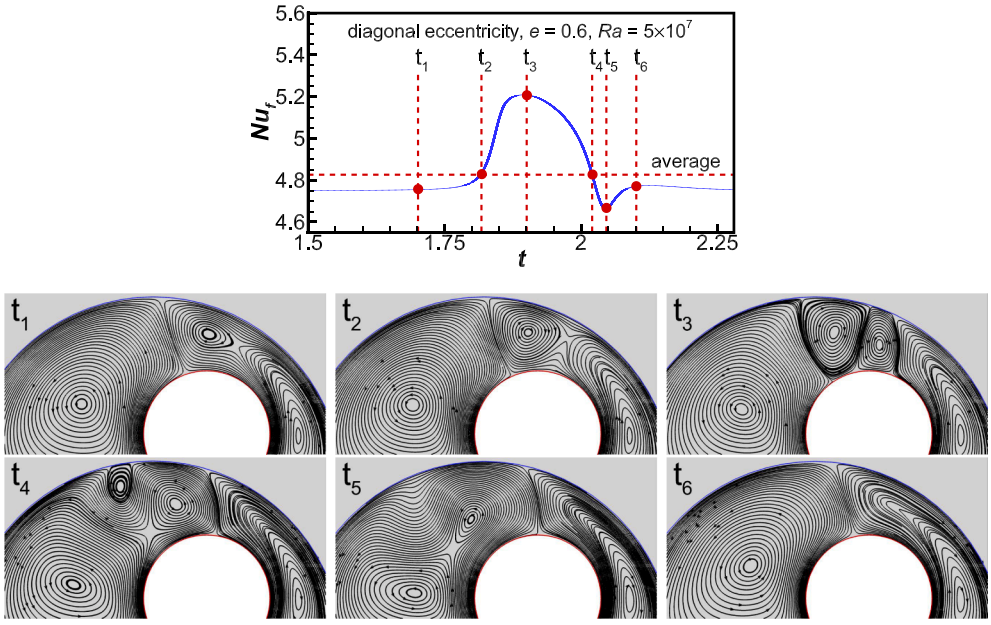

Fig. 14. Details of flow behaviour for the case of diagonal eccentricity at $e = 0.6$ and Ra $= 5\times10^7$ shown in Fig. 12, over one periodic pulse at the times indicated by red circular points.

reduction of local gap thickness in the upper area of the porous layer clarify the cause of a steep increase in Nu^f.

Whereas, the effects of eccentricity on Nu^f for the horizontal geometry that are plotted in Fig. 18 show that the gain in heat transfer for this geometry can not be enhanced by changing the eccentricity, and are only slightly increased with respect to the concentric geometry. It is obvious that as Rayleigh number increases, the heat transfer curve becomes entirely insensitive to the eccentricity.

The effects of vertical, diagonal, and horizontal eccentricity locations on the conductive heat dissipation within the solid particles represented by the solid average Nusselt number Nu^s are demonstrated in Figs. 19–21, respectively. Interestingly, it is shown that the influence of the eccentricity on Nu^s in all these directions is identical. Thus, maximum savings in Nu^s is occurred at $e = 0$, and as the eccentricity is increased in either the positive or the negative direction, Nu^s increases. see Fig. 20.

Some numerical results are presented in Fig. 22 in the form of streamlines and isotherms to show the effect of eccentricity at different positions under the three scenarios: vertical, diagonal, and horizontal eccentric configurations, at Ra $= 8 \times 10^7$. One can see that moving the inner cylinder vertically or diagonally upward forms an obstruction region to the ascending convective flow causing it to slow upstream of the porous annular layer and to accelerate downstream. This perturbation promotes a drop in the temperature gradient in the upstream proximity of the inner cylinder and an increase in the downstream vicinity. However, when the inner cylinder reaches the higher location at

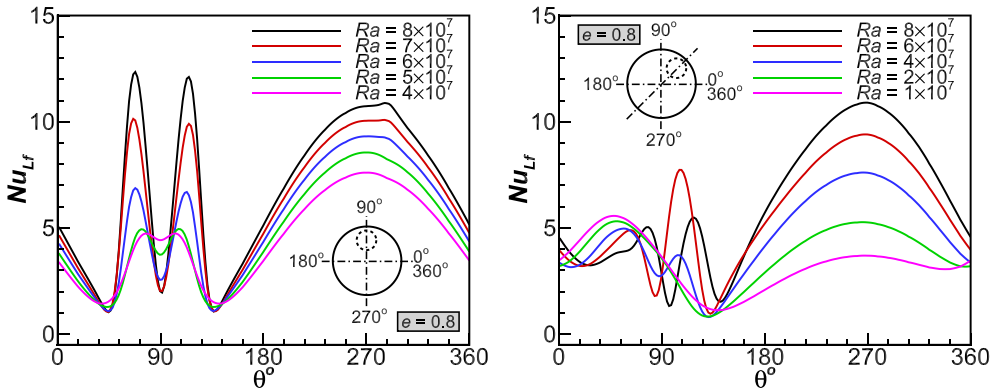

Fig. 15. Variation of Nu_{Lf} around the interior cylinder surface, at various Ra, at highest positive (Left) vertical and (Right) diagonal, eccentricities $e = 0.8$.

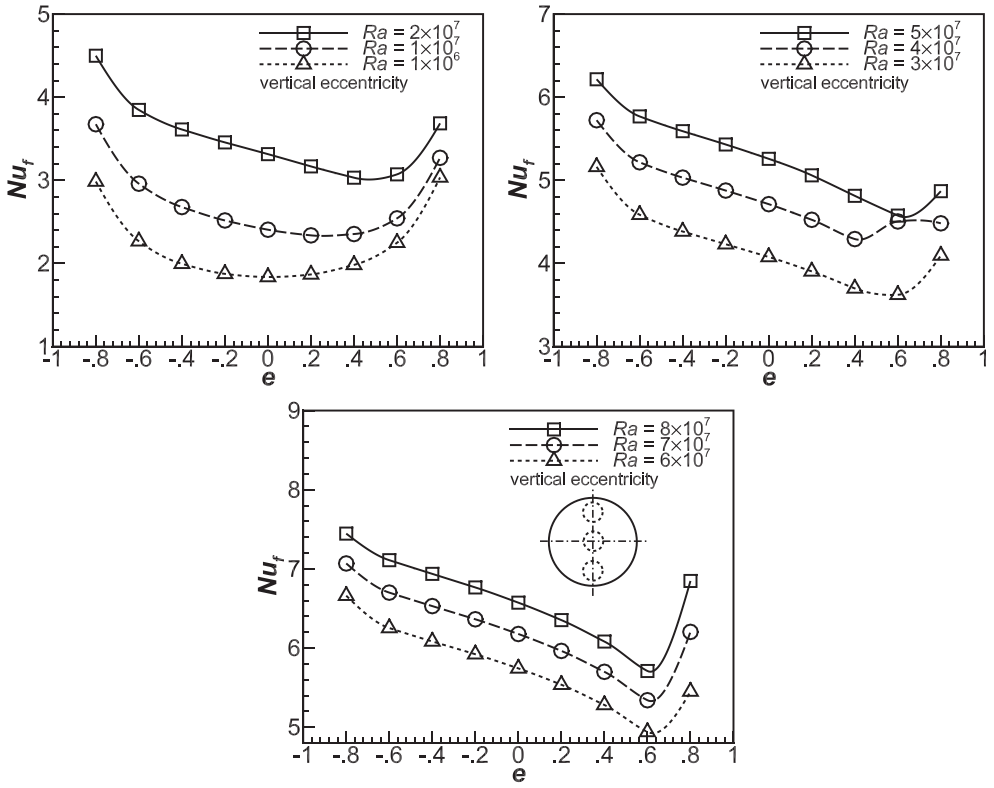

Fig. 16. Variation of Nu^f versus the vertical eccentricity at various Ra.

$e = 0.8$, the gap thickness in the upper region becomes very small, hindering the occurrence of small secondary counter-rotating cells relative to the primary one. Hence, a transition in the flow structure between the uni-cellular into the tri-cellular occurs in the vertical eccentric configuration at this higher Rayleigh number. This clarifies the steep increase in Nu^f shown in Fig. 16. At this position, moving the cylinder angularly clockwise by 45° deforms the structure of the tri-cellular flow. Then, by shifting the inner cylinder further clockwise by 45°, the secondary counter-rotating cells disappear altogether. The deformation and destruction of the secondary counter-rotating eddies result in an overall reduction in Nu^f as illustrated in Figs. 16–18 at higher $e = 0.8$ and higher $Ra = 8 \times 10^7$. From the thermal fields, an interesting plume behaviour is shown that the plume shifts in a clockwise or anti-clockwise directions as the horizontal eccentricity decreases or increases, respectively.

The results reported in Figs. 23 and 24 offer an alternative technique for optimising the rates of heat dissipation by an appropriate selection of the annular radius ratio. Fig. 23 displays the variations of average fluid Nusselt number Nu^f and solid Nusselt number Nu^s as a function of the radius ratio, six values namely RR = 1.5, 2, 2.5, 3, 4 and 5, of a concentric annular configuration, for different Rayleigh numbers. It can be noticed from the plots that the impact of radius ratio on Nu^f relies greatly on Rayleigh number. Thus, for small Rayleigh numbers (i.e. $Ra \leq 10^6$), where the pure conduction mode of heat transfer is the dominant, the increase in the porous layer thickness (RR) results in a considerable decrease in Nu^f (i.e. reduction in heat loss).

However, interestingly, as Rayleigh number increases, where the natural convection turns to be significant, there is an optimal value of the porous layer thickness appears for minimum Nu^f. This critical value is shown to decrease as Rayleigh number increases. For instance, at $Ra = 1 \times 10^7$ and 2×10^7, the critical thickness values are $RR_{(cr)} = 3$ and 2.5, respectively, and for $Ra = (3–7) \times 10^7$, $RR_{(cr)} = 2$. For the highest $Ra = 8 \times 10^7$, it is noticed that the useful insulation radius ratio turns to be the smaller one (lesser thickness). In addition, Fig. 23 shows that as

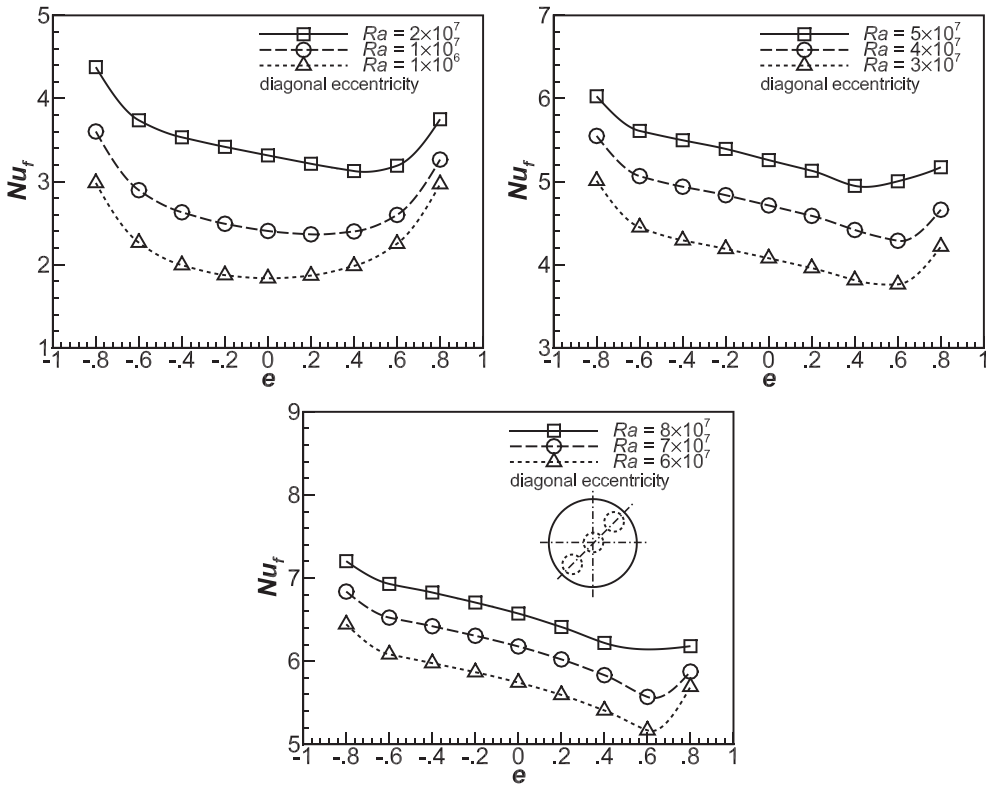

Fig. 17. Variation of Nu^f versus the diagonal eccentricity at various Ra.

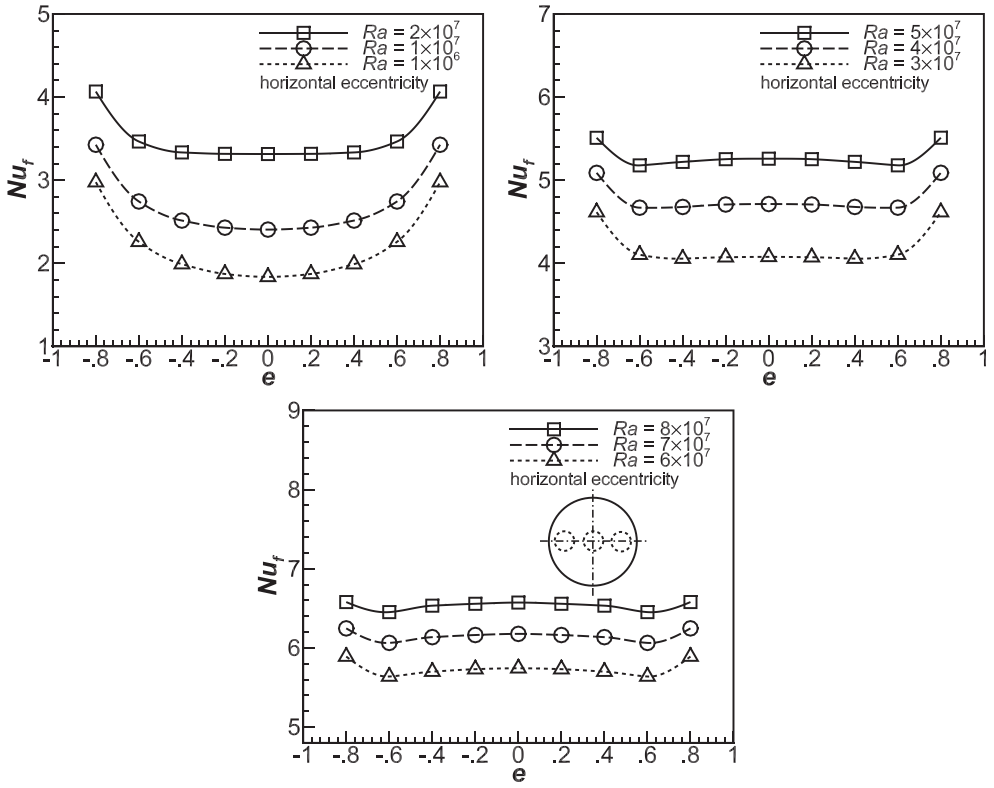

Fig. 18. Variation of Nu^f versus the horizontal eccentricity at various Ra.

the porous layer thickness is increased by increasing the annular radius ratio the conductive heat loss Nu^s during the solid spheres are reduced regardless the value of Rayleigh number.

Fig. 24 depicts another observation for the effect of radius ratio on the heat dissipation. It shows the variation of the total average Nusselt number Nu_t against Rayleigh number for the aforementioned six radius

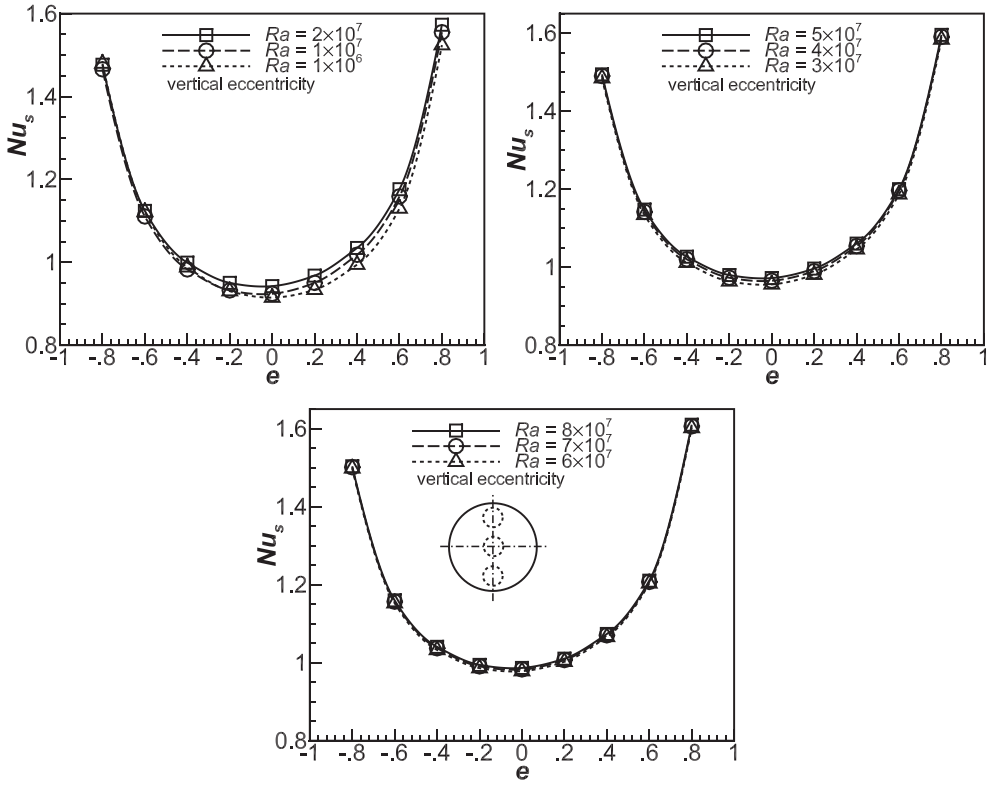

Fig. 19. Variation of Nu^s versus the vertical eccentricity at various Ra.

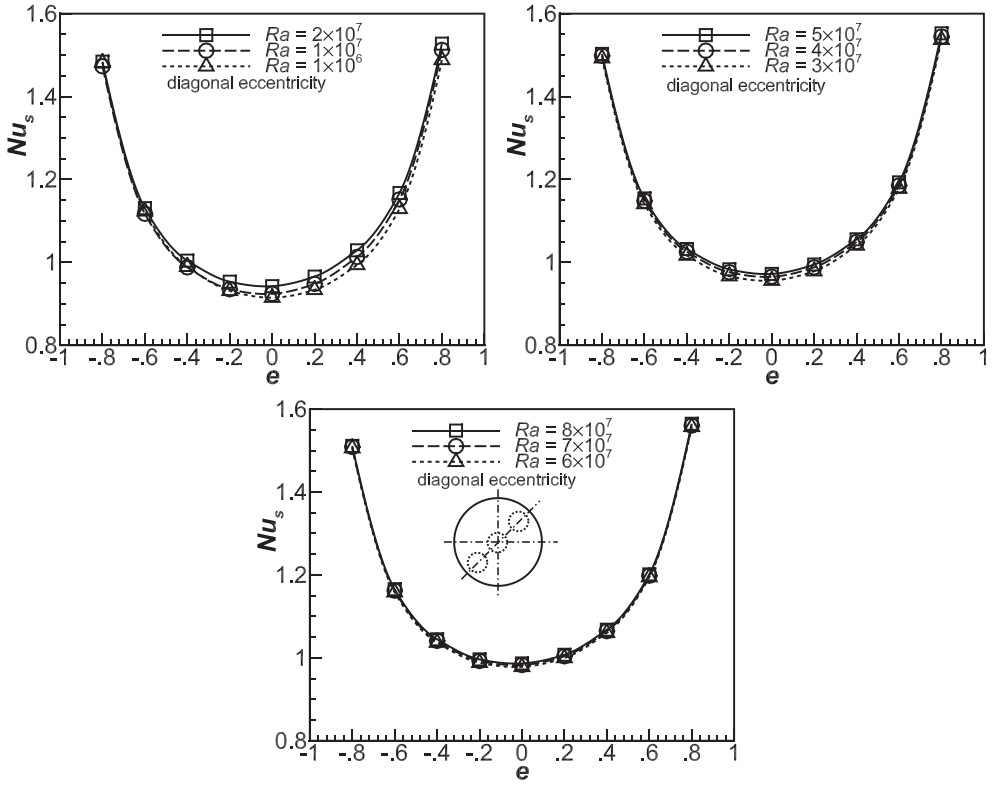

Fig. 20. Variation of Nu^s versus the diagonal eccentricity at various Ra.

ratios. It is shown that much bigger rates of heat transfer is obtained at smaller radius ratio for all Rayleigh numbers. Nevertheless, for very higher Rayleigh numbers, the influence of radius ratio reduces, hence, any value of radius ratio can achieve higher Nu_t. Also, it is shown that for low and moderate Rayleigh numbers, the figure recommends bigger annular radius ratio for thermal insulation purposes.

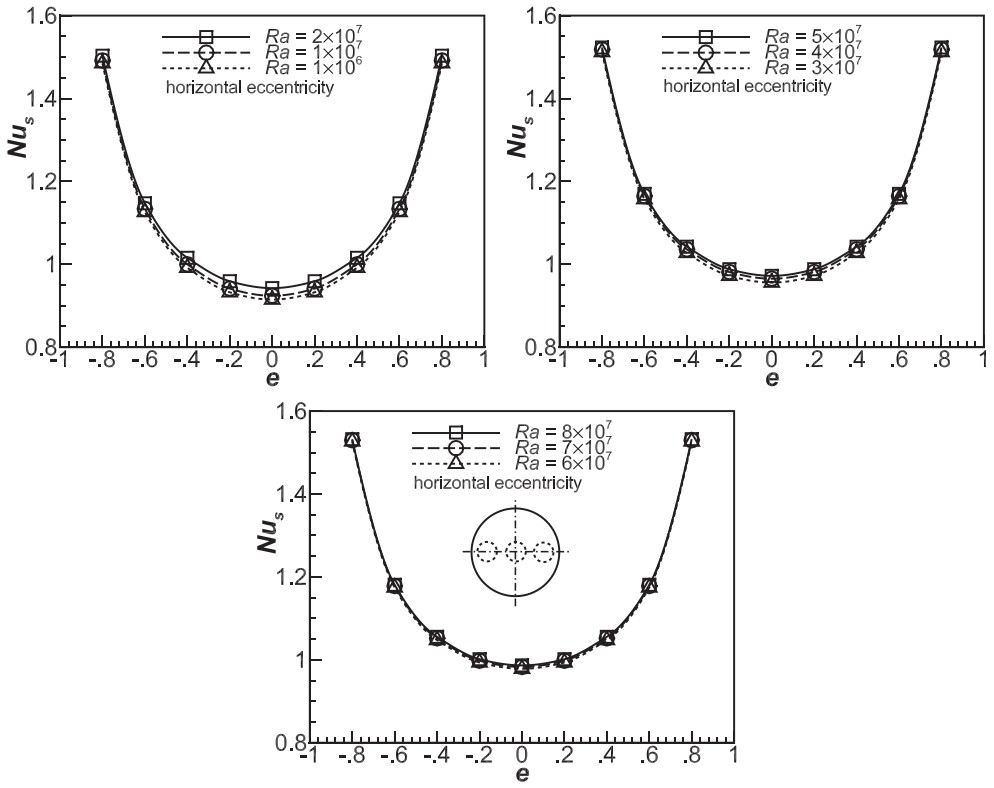

Fig. 21. Variation of Nu^s versus the horizontal eccentricity at various Ra.

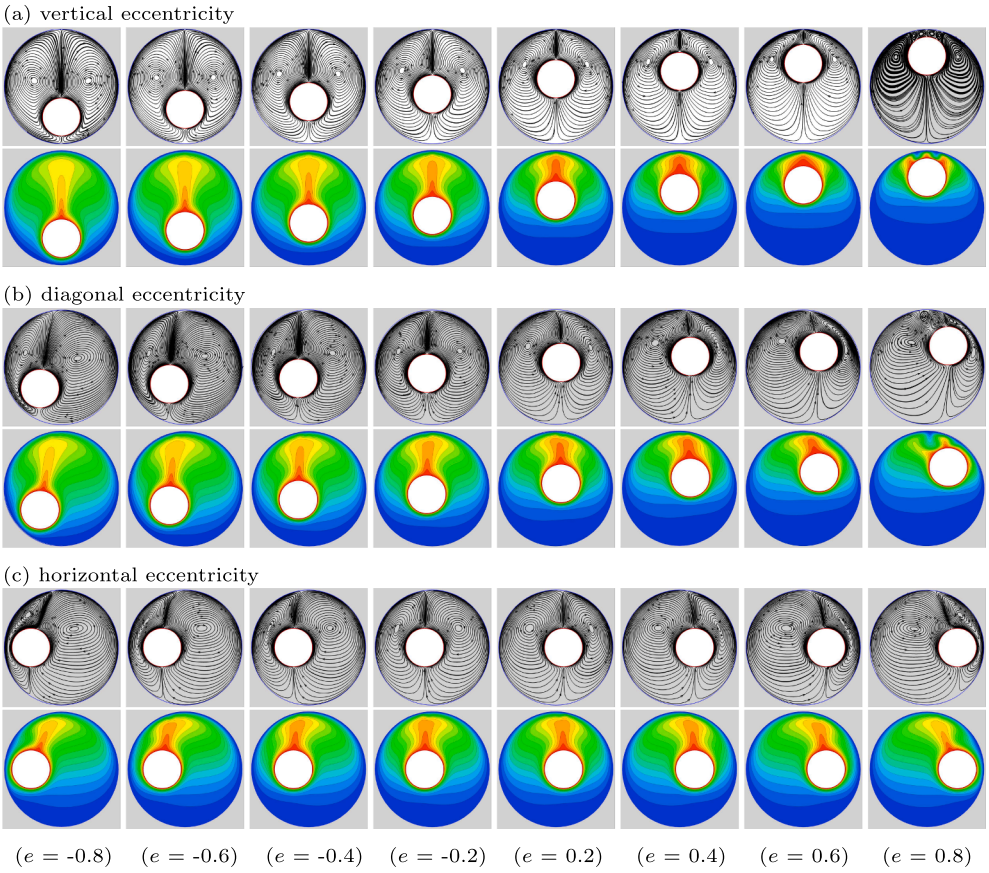

Fig. 22. Effect of (a) vertical, (b) diagonal, and (c) horizontal, eccentricities on flow and thermal patterns, at Ra = 8×10^7.

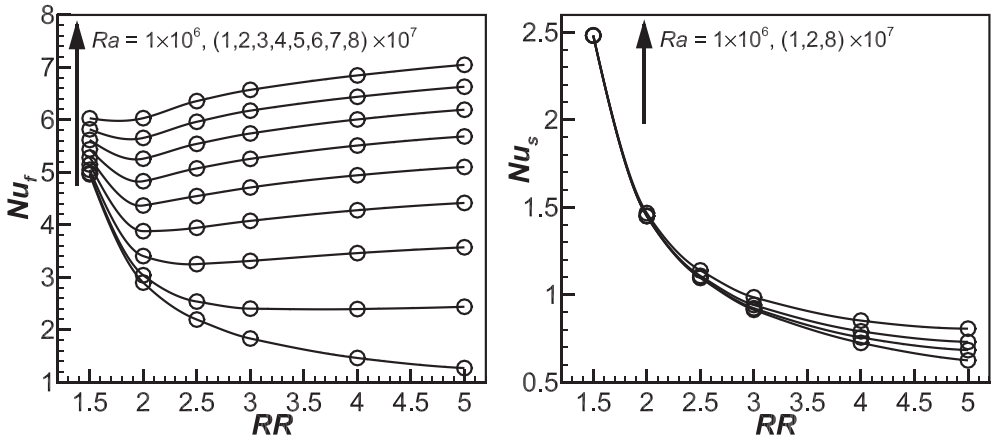

Fig. 23. Variations of fluid (Left) and solid (Right) mean Nusselt numbers with Ra, for various RR.

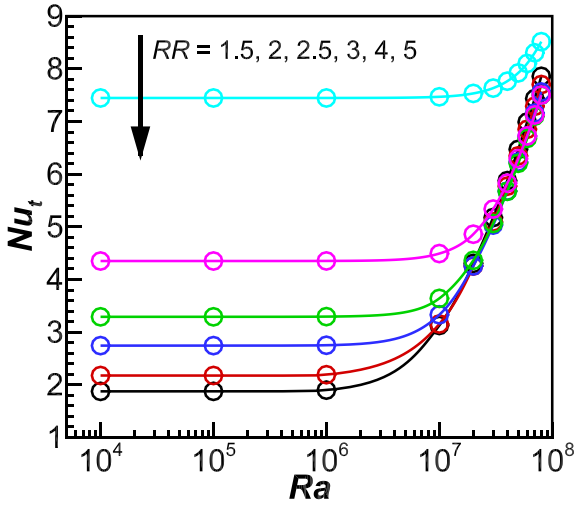

Fig. 24. Variation of total mean Nusselt number with Ra, for various RR.

The flow and thermal fields in the porous concentric annulus for different radius ratio, RR = 1.5, 2, 2.5, 3, 4 and 5, are illustrated in Fig. 25 at Ra = 1 × 10^6, 1 × 10^7, and 8 × 10^7. When the porous layer is thinner, it is seen that the fluid moves parallel to the internal walls as a result of the central zone between the two hydrodynamic boundary layers being quite slender. As a consequence of the thin thickness of the porous layer, the conduction heat dissipation is the dominant mode in the entire annulus for all Rayleigh numbers. However, increasing the porous layer width and Rayleigh number strengthens the free convection and make it prevailing in the top portion of the annulus. Hence, this causes concentric isotherms, such are almost consistently distributed, moving strongly upward generating a high temperature gradient in the lower region of the annulus, and producing a strong thermal plume in the upper region. It is noticed that reducing the radius ratio to the small value of RR = 1.5 is not hindering the appearance of secondary cells in the top portion of the annulus. It is concluded that within the range of radius ratio investigated here, multi-cellular flow structures can not be occurred even at very high Rayleigh numbers. Indeed, this behaviour is dissimilar to that seen in the vertical or diagonal eccentric geometries with very high eccentricity.

7. Conclusions

In this study, natural convection and heat transfer between two horizontal concentric and eccentric cylinders filled with spherical particles as a porous medium saturated by air is investigated numerically. Characteristics of flow and heat transfer are studied for a broad range of pertinent parameters of the problem: The eccentricity ($-0.8 \leqslant e \leqslant 0.8$) in vertical, diagonal and horizontal directions, the annulus radius ratio ($1.5 \leqslant RR \leqslant 5.0$) and Rayleigh number ($10^4 \leqslant Ra \leqslant 8 \times 10^7$). The following conclusions are drawn from the present results:

1. The average fluid Nusselt number (Nu^f) is not affected by Rayleigh number for Ra $\leq 10^7$ in the vertical, diagonal and horizontal eccentric annuli. However, for Ra $> 10^7$, Nu^f increases significantly with Rayleigh number. The heat transfer performance of the vertical and diagonal configurations is much better than that for the horizontal one.
2. In the vertical eccentric annulus, only uni-cellular flow regime is seen at $e = -0.8$ for all Rayleigh numbers, however, at $e = 0.8$, uni-cellular, bi-cellular, and tri-cellular are seen, as Rayleigh number increases. In the diagonal eccentric annulus, the multi-cellular flow regimes are deformed and the isotherms are particularly distorted when Rayleigh number increases.
3. In the diagonal eccentric annulus, the fluid flow is significantly unstable at $e = 0.8$ for Ra $\geqslant 4 \times 10^7$, and becomes stable as Rayleigh number decreases below 4×10^7, or as the eccentricity decreases under $e = 0.8$. However, in the vertical eccentric annulus, interestingly, it loses the stability only at two cases when $e = 0.8$ at Ra $= 7 \times 10^7$ and when $e = 0.6$ at Ra $= 5 \times 10^7$.
4. For low Rayleigh numbers, the concentric insulation is the most effectual one amongst the three eccentric configurations considered, while the better heat transfer enhancer is in the eccentric annuli at larger negative and positive eccentricities. However, for large Rayleigh numbers, in the vertical and diagonal eccentric configurations, there is an optimal value of eccentricity at $e = 0.6$ for better effectively eccentric insulation than concentric one.
5. The effect of porous layer thickness (radius ratio RR) on Nu^f depends on Rayleigh number. Thus, for low Ra, Nu^f decreases as RR increases; however, for large Ra, a critical value of RR is obtained for getting minimum Nu^f, while, for very high Ra, the useful insulation RR turns to be the smaller one.
6. The reduction in RR to the smaller values is not hindering the appearance of secondary cells in the upper region of the annulus, and multi-cellular flow structures could not be observed even at very high Rayleigh numbers.

Funding

This research did not receive any specific grant from funding agencies in the public, commercial, or not-for-profit sectors.

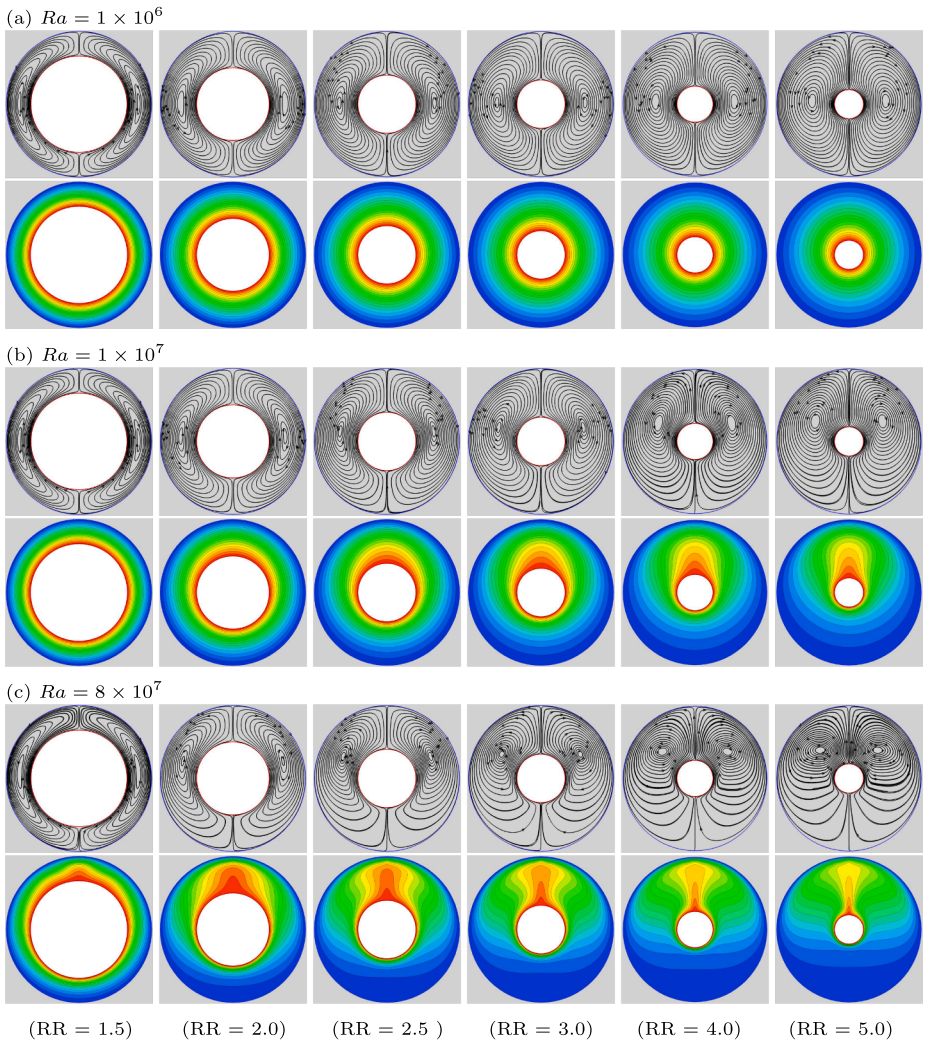

Fig. 25. Effect of annuli radius ratio RR = r_o/r_i on flow and thermal patterns at (a) Ra = 1×10^6, (b) Ra = 1×10^7, and (c) Ra = 8×10^7.

CRediT authorship contribution statement

Gazy F. Al-Sumaily: Conceptualization, Methodology, Investigation, Visualization. **Hasanen M. Hussen:** Writing - original draft, Writing - review & editing. **Wissam H. Alawee:** Data curation, Formal analysis. **Hayder A. Dhahad:** Project administration, Resources. **Mark C. Thompson:** Software, Validation, Supervision.

Declaration of Competing Interest

The authors declare that they have no known competing financial interests or personal relationships that could have appeared to influence the work reported in this paper.

Acknowledgements

This research was supported in part by the Monash eResearch Centre and eSolutions-Research Support Services through the use of the MonARCH HPC Cluster.

References

Hakan, F.O., 2007. Natural convection in partially cooled and inclined porous rectangular enclosures. Int. J. Therm. Sci. 46, 149–156.
Hakan, F.O., Yasin, V., Ioan, P., 2009. Investigation of natural convection in triangular enclosure filled with porous media saturated with water near 4 °C. Energy Convers. Manage. 50, 1473–1480.
Selimefendigil, F., Hakan, F.O., 2017. Conjugate natural convection in a nanofluid filled partitioned horizontal annulus formed by two isothermal cylinder surfaces under magnetic field. Int. J. Heat Mass Transfer 108, 156–171.
Nadezhda, S.B., Mikhail, A.S., Hakan, F.O., Nidal, A., 2017. Entropy generation due to natural convection of a nanofluid in a partially open triangular cavity. Adv. Powder Technol. 28, 244–255.
Walid, H., Hakan, F.O., Lioua, K., Mohamed, N., Nidal, A., 2017. Analysis of the electro-thermo-convection induced by a strong unipolar injection between two concentric or eccentric cylinders. Numer. Heat Transfer A 71 (7), 789–804.
Schwalp, T.H., de Witt, K.J., 1970. Numerical investigation of free convection between two vertical coaxial cylinders. AIChE J. 16, 1005–1010.
Powe, R., Corley, C., Carrath, S., 1971. A Numerical solution for natural convection in cylindrical annuli. J. Heat Transfer 93, 210–220.
Custer, J.R., Shaughnessy, E.J., 1977. Natural convection in liquid metals in an enclosure. J. Heat Transfer 99, 675–676.
Charrier-Mojtabi, M.C., Mojtabi, A., Caltagirone, J.P., 1979. Numerical solution of a flow due to natural convection in horizontal cylindrical annulus. J. Heat Transfer 101, 171–173.
Keivan, F., Atena, G., Nima, S., Mohammad Hossein, B., 2017. Simulation of natural convection heat transfer using nanofluid in a concentric annulus. Therm. Sci. 21, 1275–1286.
Koichi, H., Toshitaka, H., Youji, I., 2001. Natural convection heat transfer in eccentric horizontal annuli between a heated outer tube and a cooled inner tube with different orientation: the case of an elliptical outer tube. Heat Transfer-Asian Res. 30.
Kuehn, N.H., Goldstein, R.J., 1976. Correlating equations for natural convection heat transfer between horizontal circular cylinders. Int. J. Heat Mass Transfer 10, 1127–1134.
Ratzel, A.C., Hickox, C.E., Gartling, D.K., 1979. Techniques for reducing thermal conduction and natural convection heat losses in annular receiver geometries. J. Heat Transfer 101, 108–113.
Yao, L.S., 1980. Analysis of heat transfer in slightly eccentric annuli. J. Heat Transfer 102, 279–284.

Projahn, V., Reiger, H., Beer, H., 1981. Numerical analysis of laminar natural convection between concentric and eccentric cylinders. Numer. Heat Transfer 4, 131–146.
Feldman, E.E., Hornbeck, R.W., Osterle, J.F., 1982. Numerical solution of laminar developing flow in eccentric annular ducts. Int. J. Heat Mass Transfer 25, 131–241.
Ho, J., Lin, Y.H., Chen, T.C., 1989. A numerical study of natural convection in concentric and eccentric horizontal cylindrical annuli with mixed boundary conditions. Int. J. Heat Fluid Flow 10, 40–47.
Hwang, T.H., Jensen, M.K., 1991. An analysis of convective heat transfer to laminar dispersed flow in eccentric annuli. Int. Commun. Heat Mass Transfer 18, 27–38.
Hosseini, R., Heyrani-Nobari, M.R., Hatam, M., 2005. An experimental study of heat transfer in an open-ended vertical eccentric annulus with insulated and constant heat flux boundaries. Appl. Therm. Eng. 25, 1247–1257.
Caltagirone, J.P., 1976. Thermoconvective instabilities in a porous medium bounded by two concentric horizontal cylinders. J. Fluid Mech. 76, 337–362.
Rao, Y.F., Fukuda, K., Hasegawa, S., 1987. Steady and transient analyses of natural convection in a horizontal porous annulus with the Galerkin method. ASME J. Heat Transfer 109, 919–927.
Rao, Y.F., Fukuda, K., Hasegawa, S., 1988. A numerical study of three-dimensional natural convection in a horizontal porous annulus with Galerkin method. Int. J. Heat Mass Transfer 31, 695–707.
Himasekhar, K., Bau, H.H., 1988. Two-dimensional bifurcation phenomena in thermal convection in horizontal, concentric annuli containing saturated porous media. J. Fluid Mech. 187, 267–300.
Charrier-Mojtabi, M.C., Mojtabi, A., Azaiez, M., Labrosse, G., 1991. Numerical and experimental study of multicellular free convection flows in an annular porous layer. Int. J. Heat Mass Transfer 34, 3061–3074.
Barbosa Mota, J.P., Saatdjian, E., 1992. Natural convection between two horizontal porous cylinders. Adv. Comput. Methods Heat Transfer 2, 393–401.
Barbosa Mota, J.P., Saatdjian, E., 1994. Natural convection in a porous, horizontal cylindrical annulus. ASME J. Heat Transfer 116, 621–626.
Barbosa Mota, J.P., Saatdjian, E., 1995. Natural convection in porous cylindrical annuli. Int. J. Numer. Methods Heat Fluid Flow 5, 3–12.
Bau, H.H., 1984. Low Rayleigh number thermal convection in a saturated porous medium bounded by two horizontal eccentric cylinders. J. Heat Transfer 106, 166–175.
Bau, H.H., 1984. Thermal convection in a horizontal eccentric annulus containing saturated porous medium – an extended perturbation expansion. Int. J. Heat Mass Transfer 27, 2277–2287.
Himasekhar, K., Bau, H.H., 1986. Large Rayleigh number convection in a horizontal, eccentric annulus containing saturated porous media. Int. J. Heat Mass Transfer 29, 703–712.
Barbosa Mota, J.P., Saatdjian, E., 1997. On the reduction of natural convection heat transfer in horizontal eccentric annuli containing saturated porous media. Int. J. Numer. Methods Heat Fluid Flow 7, 401–416.
Barbosa Mota, J.P., Saatdjian, E., 1994. Natural convection in a porous, horizontal cylindrical annulus. ASME J. Heat Transfer 116, 621–626.
Barbosa Mota, J.P., Esteves, I.A., Portugal, C.A., Saatdjian, E., 2000. Natural convection heat transfer in horizontal eccentric elliptic annuli containing saturated porous media. Int. J. Heat Mass Transfer 43, 4367–4379.
Slattery, J.C., 1967. Flow of viscoelastic fluids through porous media. AIChE J. 13 (6), 1066–1071.
Whitaker, S., 1967. Diffusion and dispersion in porous media. AIChE J. 13 (3), 420–427.
Vafai, K., Sozen, M., 1994. nalysis of energy and momentum transport for fluid flow through a porous bed. J. Heat Transfer Trans. ASME 112, 690–699.
Amiri, A., Vafai, K., 1994. Analysis of dispersion effects and non-thermal equilibrium, non-Darcian, variable porosity incompressible flow through porous media. Int. J. Heat Mass Transfer 37, 939–959.
Zehner, P., Schluender, E.U., 1970. Thermal conductivity of granular materials at moderate temperatures. Chem. Ing. Techn. 42 (14), 933–941.
Ergun, S., 1952. Fluid flow through packed columns. Chem. Eng. Prog. 48 (2), 89–94.
Darrell, W.P., Roger, E.C., 1983. Numerical solution of natural convection in eccentric annuli. AIAA J. 21.
Dullien, F.A., 1979. Media Fluid Transport and Pore Structure. Academic Press, New York.
Wakao, N., Kaguei, S., Funazkri, T., 1979. Effect of fluid dispersion coefficients on particle-to-fluid heat transfer coefficients in packed beds- correlation of Nusselt numbers. Chem. Eng. Sci. 34 (3), 325–336.
Karniadakis, G., Israeli, M., Orszag, S., 1991. High-order splitting methods of the incompressible Navier-Stokes equations. J. Comput. Phys. 97, 414–4430.
Thompson, M.C., Hourigan, K., Cheung, A., Leweke, T., 2006. Hydrodynamics of a particle impact on a wall. Appl. Math. Model. 30, 1356–1369.
Chorin, A.J., 1968. Numerical solution of the navier-stokes equations. Math. Comput. 104 (22), 745–762.
Fletcher, C.A.J., 1984. Computational Galerkin Methods. Springer-Verlag, New York.
Fletcher, C.A.J., 1991. Computational Techniques for Fluid Dynamics, vol. 1. Springer-Verlag, New York.
Karniadakis, G.E., Sherwin, S.J., 2005. Spectral/hp) Methods for Computational Fluid Dynamics. Oxford University Press, Oxford.
Al-Sumaily, G., John, S., Thompson, M.C., 2012. Analysis of forced convection heat transfer from a circular cylinder embedded in a porous medium. Int. J. Therm. Sci. 51, 121–131.
Al-Sumaily, G., Thompson, M.C., 2013. Forced convection from a circular cylinder in pulsating flow with and without the presence of porous media. Int. J. Heat Mass Transfer 61, 226–244.
G. Al-Sumaily, Forced convection heat transfer from a bank of circular cylinders embedded in a porous medium, J. Heat Transfer ASME 136 (4) (2014) 042602-042602-11.
Al-Sumaily, G., 2014. Bénard convection from a circular cylinder in a packed bed. Int. Commun. Heat Mass Transfer 54, 18–26.
Cheng, P., 1982. Mixed convection about a horizontal cylinder and a sphere in a fluid-saturated porous medium. Int. J. Heat Mass Transfer 25 (8), 1245–1247.
Nasr, K., Ramadhyani, S., Viskanta, R., 1994. Experimental investigation on forced convection heat transfer from a cylinder embedded in a packed bed. J. Heat Transfer 116 (1), 73–80.
Kumari, M., Jayanthi, S., 2004. Non-Darcy non-Newtonian free convection flow over a horizontal cylinder in a saturated porous medium. Int. Commun. Heat Mass Transfer 31 (8), 1219–1226.
Pop, I., Kumari, M., Nath, G., 1992. Free convection about cylinders of elliptic cross section embedded in a porous medium. Int. J. Eng. Sci. 30 (1), 35–45.
Yih, K., 1999. Coupled heat and mass transfer by natural convection adjacent to a permeable horizontal cylinder in a saturated porous medium. Int. Commun. Heat Mass Transfer 26 (3), 431–440.